https://doi.org/10.5194/egusphere-2026-933
Preprint. Discussion started: 6 March 2026

Atmospheric circulation and boundary layer processes modulating aerosol and cloud characteristics over the coastal Northeast Pacific during April to October of ARM EPCAPE field campaign

Seethala Chellappan[1,2], David Painemal[2], Mandana Thieman[2,3], Christian Pelayo[4], William L. Smith Jr.[2], and Lynn M Russell[4]

[1]Analytical Mechanics Associates, Hampton, Virginia, USA
[2]NASA Langley Research Center, Hampton, Virginia, USA
[3]ADNET, Hampton, Virginia, USA
[4]Scripps Institution of Oceanography, University of California San Diego, La Jolla, California, USA

Correspondence to: seethala.chellappan@nasa.gov

Abstract. Observations from the ARM Eastern Pacific Cloud Aerosol Precipitation Experiment (EPCAPE) spanning April to October 2023 at Scripps Pier, La Jolla, California (32.8663°N, 117.2546°W) were used to investigate the regional-scale atmospheric factors that control the variability of marine low clouds and aerosols in the coastal boundary layer (BL). Using Self-Organizing Maps applied to ERA5 sea level pressure and near-surface winds, we classify the synoptic evolution of the subtropical anticyclone into 9 regimes, which includes: 1) patterns with a weakened subtropical anticyclone south of Scripps Pier and a midlatitude cyclone further north, 2) regimes that capture the evolution of anticyclone in terms of magnitude (strong vs weak) and location (coastal vs offshore), with their corresponding transitions in BL wind strengthening and large-scale subsidence, 3) a regime characterized by an anticyclone with its core at the northwestern edge of the domain, and 4) a regime that captures anomalies that minimally depart from the climatological mean. GOES-18 cloud retrievals reveal that regimes associated with anticyclone cores closer to Scripps Pier produce reduced low-cloud fraction, shallower clouds, and low liquid water path (LWP); whereas regimes with a west/north-westward-displaced anticyclone support extensive stratocumulus with higher LWP and elevated cloud tops. Regimes with a weak anticyclone centered adjacent to the Pier feature highest concentrations of smaller-sized particles, associated with a stable BL and stagnation under weak winds. Regimes with anticyclonic

https://doi.org/10.5194/egusphere-2026-933
Preprint. Discussion started: 6 March 2026

strengthening farther-offshore have lower aerosol concentrations. Partial inconsistency between cloud droplet number concentration (N_d) and aerosol concentration indicates BL turbulence critically influences aerosol activation into N_d.

1. Introduction

The Northeast Pacific stratiform cloud regime is a key climatological feature over the subtropics, playing a central role on the Earth's radiation budget (Hartmann et al., 1992; Wood, 2012) and exerts a climate feedback with the large-scale sea surface temperature and atmospheric circulation (e.g., Clement et al., 2009). Coastal Southern California experiences diverse synoptic weather patterns driven by the coastal topography and large-scale circulation. The subtropical high dominates in spring and summer, generating strong onshore flow that enhances marine layer clouds and coastal cooling (Raphael, 2003; Clemesha et al., 2017). In contrast, fall and winter witness a wider range of weather patterns, with frequent synoptic-scale transitions of anticyclonic and cyclonic circulation of varying extent and magnitude. These changes dramatically modulate cloud variability, giving rise to convective systems especially in frontal regions, and synoptically-forced stratocumulus clouds under conditions with strong post-cyclonic subsidence (Weaver and Ramanathan, 1994). Fall and winter also bring offshore-directed Santa Ana winds, transporting warmer and drier air towards the coast, favoring dust and smoke from wildfires far out over the Ocean (Abel and Hall, 2010). These circulation shifts generate stark contrasts in coastal meteorology, pollutant dispersion, and cloud variability (Lu and Turco, 1994, 1995). Furthermore, the diurnal land-sea breeze interacts with the synoptic forcing. Weak synoptic forcing allows land-sea breezes to dominate, while katabatic winds originated from a high-pressure system (Santa Ana winds) disrupt these cycles, enhancing offshore pollutant transport and reducing cloud coverage (Abel and Hall, 2010). In contrast, low-pressure conditions strengthen the offshore flow, deepen the marine atmospheric boundary layer (MBL), and increase the cloud cover (Lebassi-Habtezion et al., 2011).

The coastal southern California is particularly impacted by transport of polluted air from industrial regions like Los Angeles and Long Beach (Husar and Patterson, 1980; Husar et al., 1977). Moreover, pollution transport extends offshore over the stratocumulus cloud-topped marine atmospheric boundary layer during Santa Ana wind events (Abel and Hall, 2010), directly affecting the marine stratocumulus clouds. Conversely, synoptic onshore flow brings pristine

https://doi.org/10.5194/egusphere-2026-933
Preprint. Discussion started: 6 March 2026

marine aerosols inland, dramatically changing the local aerosol composition (Maneenoi et al., 2025; Han et al., 2025). The diversity in chemical composition and wide range of aerosol variability makes this region a unique observatory for investigating aerosol pathways and modes of variability over a coastal region situated next to densely urbanized areas. Moreover, advection of continental aerosols over the adjacent ocean can potentially impact the evolution and radiative properties of the NE Pacific stratocumulus cloud deck. In this respect, a fundamental mechanism of aerosol-cloud interaction is through an increase in cloud droplet number concentration (N_d) mediated by an increase of cloud condensation nuclei (CCN) under conditions of enhanced aerosol loading (Bellouin et al., 2020 and references therein). The positive correlation between CCN and N_d have been observed in several studies (e.g., Sorooshian et al., 2019; Painemal et al., 2017), with the radiative implications manifested in an increase of albedo at the top of the atmosphere documented from satellite observations (Painemal, 2018). It has been hypothesized that changes in N_d can trigger multiple feedbacks and rapid cloud adjustments that can alter the cloud properties (precipitation, water content, thickness, among other); however, their magnitudes remain highly uncertain (Bellouin et al., 2020).

An important factor contributing to uncertainties in the quantification of the aerosol indirect effect is the fact that clouds primarily respond to changes in the local atmospheric state, which in turn also modulate the microphysical interactions between aerosol and clouds. Indeed, Chen et al. (2014) and Zhang et al. (2022) highlight the importance of accounting for meteorological factors for assessing aerosol-cloud interactions (e.g., atmospheric stability and humidity). For the NE Pacific, data collected during the MAGIC campaign (Lewis, 2016) along with reanalyzed meteorological fields show the importance of the coastal California low-level jet as a key mechanism transporting aerosols from North American continent to the northeast Pacific. Furthermore, Painemal et al. (2015) found a negative correlation between 1000 hPa zonal wind and N_d, underscoring the influence of large-scale meteorology in transporting aerosol from coastal regions to the open ocean in the NE Pacific.

Cognizant of the knowledge gaps in the characterization of clouds and aerosols in the atmospheric boundary layer of coastal California, the Department of Energy's Atmospheric Radiation Measurement (ARM) program deployed the ARM Mobile Facility at Scripps Pier (32.8663°N, 117.2546°W) in La Jolla (California) during the Eastern Pacific Cloud Aerosol Precipitation Experiment (EPCAPE; Russell et al., 2025). This year-long field campaign, conducted from mid-February 2023 to mid-February 2024, provided comprehensive high-resolution observations of aerosols, clouds, precipitation, and atmospheric state. Being a downwind coastal site, Scripps Pier is ideally situated to observe the interactions between continental and marine air masses, and boundary layer clouds in the NE Pacific.

Here, we describe the synoptic regimes that modulate cloud variability and aerosol characteristics over the coastal Southern California for the period spanning April through October, 2023 corresponding to a period characterized by the frequent presence of stratocumulus clouds. To this end, we employ self-organizing maps (SOM) – an unsupervised neural network method – to categorize meteorological regimes using fields from the Fifth Generation ECMWF reanalysis (ERA5). In addition, SatCORPS satellite clouds retrievals from the 18th Generation Geostationary Operational Environment Satellite (GOES-18) and ground-based in-situ and remote sensing measurements for the study period from the EPCAPE campaign at Scripps Pier are combined to analyze the factors that link the atmospheric circulation with cloud and aerosol characteristics. By leveraging EPCAPE observations, this research provides a novel approach to linking large-scale weather patterns with localized atmospheric processes. The paper is structured as follows: Section 2 outlines the EPCAPE in-situ and remote measurements, satellite cloud observations, and reanalysis data. Section 3 covers atmospheric regime classification using SOM. Section 4 describes meteorological, cloud, and aerosol properties within these atmospheric regimes. Section 5 outlines the summary and discussion.

2. Datasets and methodology

The key dataset for this study was collected by the ARM's Mobile Facility deployed at Scripps Pier during EPCAPE. ERA5 and SatCORPS GOES-18 are primarily used for describing the regional scale context of the EPCAPE observations. In the following, we describe the dataset used in our study.

2.1. ARM observations and products

Cloud boundaries

Cloud base height (CBH) is estimated from a laser ceilometer Vaisala CL31 (CEIL; Morris, 2016), with a 16-s sampling and a vertical resolution of 10 m. The typical accuracy of CBH measurements is within ±30 meters for low clouds, though uncertainties increase at higher altitudes or in the presence of fog, aerosols, or precipitation. Ceilometer data were also used to estimate the hourly cloud occurrence frequency for low altitude clouds, hereafter referred to as cloud frequency fraction (CFF) and computed by counting the number of cloudy observations relative to the total sampling in an hour. At Scripps Pier, CEIL data are available for the entire campaign period, with a data gap during October 15 to November 6, 2023.

The vertically pointing Ka-band ARM Zenith Radar (KAZR, Widener et al., 2012; Feng et al., 2024), provided cloud top height (CTH) measurements throughout the campaign. We used the KAZR Active Remote Sensing of Clouds (KAZRARSCL) Value Added Product (VAP) for determining the cloud height, with the vertical resolution of 30 m and a 4-s sampling.

Liquid water path and cloud optical thickness

The 3-channel Microwave Radiometer (MWR3C) provided LWP retrievals at 1-second interval throughout the campaign. MWR3C measures brightness temperatures at three frequencies – 23.8 GHz, 30 GHz, and 89 GHz – which are sensitive to atmospheric water vapor and liquid water. The LWP is retrieved using the updated Microwave Radiometer RETrieval (MWR3RET) algorithm which follows the physical retrieval method developed by Turner et al. (2007) and Gaustad and Turner (2009) and is provided as ARM Value Added Product. The inclusion of the 89 GHz channel, with its enhanced sensitivity to low liquid water content, improves retrievals for clouds with small LWP. We limit the sampling to boundary layer clouds by only retaining observed clouds with tops below 2 km. Precipitating events are filtered out using rain flags, and uncertainty for thin clouds is minimized by removing samples with LWP < 5 g m^{-2}.

Cloud optical thickness (τ) is estimated from the ARM Cimel Sunphotometer (CSPHOT), a multi-channel automatic sun-and-sky scanning radiometer that measures direct solar irradiance and sky radiance at the surface during daylight hours. The retrieval algorithm employs non-absorbing zenith radiances at 440–870 nm for determining τ, and is available as Cloud Mode VAP (Chiu et al., 2010, 2012). Ground-based ARM N_d is computed from CSPHOT τ and MWR3RET LWP following Painemal et al. (2017), enabling robust analysis of cloud microphysical properties from ground-based data.

Aerosol observations

Continuous range of aerosol number concentration (N_a) and particle size distribution are obtained from merged Scanning Mobility Particle Sizer (SMPS) and Aerodynamic Particle Sizer

(APS) measurements, available as MERGEDSMPSAPS VAP (Beddows et al., 2010; Shilling and Levin, 2023). The SMPS measures the high-accuracy aerosol number size distribution, in the particle diameter range from 0.01 to 0.5 µm, by sizing particles based on their electrical mobility diameter using a differential mobility analyzer (DMA) and by counting particles using a condensation particle counter (CPC). The APS measures larger atmospheric particles in the diameter range of 0.5 to 20 µm, based on their aerodynamic diameter using the time-of-flight principle. Datasets are available for the entire EPCAPE time frame at 5-minutes except for a short duration (September 19 through October 23) of missing data.

Chemical composition and mass concentration of species aerosols such as organics, sulfate, nitrate, ammonium, and chloride are derived from Aerosol Chemical Speciation Monitor (ACSM: Shilling et al., 2024; Maneenoi et al., 2025) and are available at a 30 minute interval.

Cloud Condensation Nuclei

The cloud condensation nuclei (CCN) number concentration was measured on Scripps Pier by DOE ARM using a Cloud Condensation Nuclei Counter (CCN-200, DMT). The CCN counts aerosol particles after growing them at water supersaturations of 0.1%, 0.2%, 0.4%, 0.6%, 0.8%, and 1.0% during a 1-hr cycle. This dataset is available for 25 May 2023 to 14 February 2024. A scaling factor of 1.67 (Berta et al., 2025) was applied to correct for a leak upstream of the instrument inlet that diluted CCN number concentrations with air from inside the air-conditioned instrument van based on closure with composition and comparisons to the Mt. Soledad site (Dedrick et al., 2026).

Meteorological observations and models

The reanalyzed atmospheric dataset used in this study corresponds to ERA5 (Hersbach et al., 2020). ERA5 combines various observations from satellite and weather stations with advanced numerical weather prediction models to provide consistent and complete global records of atmospheric, oceanic, and land-surface conditions. Comprehensive atmospheric datasets are produced hourly at a horizontal resolution of 31 km (with spatial resolution of 0.25° × 0.25°) and 137 vertical levels extending from surface to 0.01 hPa. The hourly datasets, as well as daily and monthly mean are also available to download at 10.24381/cds.adbb2d47. The single-level products sea level pressure and sea surface temperature, as well as near-surface (975 hPa) winds, free-tropospheric (750 hPa) temperature, humidity, and winds from the vertical profiles are utilized in this study.

Backtrajectories are obtained from ARMTRAJ (Silber et al., 2025), an ARM VAP. ARMTRAJ consists of an ensemble of HYSPLIT forward and backward trajectories derived from hourly ERA5 reanalysis at 0.25˚ resolution for up to 10 days. ARMTRAJ is initialized at different levels, including surface (ARMTRAJ-SURF, 10 m), boundary layer top (ARMTRAJ-PBL), and cloud layer (ARMTRAJ-CLD). These trajectories provide information on the origin of air masses and are used to understand the source and transport path of aerosol and trace gas distributions. Here, we primarily utilize PBL trajectories to identify the possible transport processes for different atmospheric regimes at the Scripps Pier. ARM Eddy Correlation (ECOR) system provides half-hour measurements of the surface fluxes and carbon dioxide (Cook and Sullivan, 2025; Sullivan et al., 2025). The ECOR system deployed at the Scripps Pier include a fast-response, 3D wind sensor (sonic anemometer) to record the orthogonal wind components and the speed of sound, which is used to derive the air temperature, and an open-path infrared gas analyzer (IRGA) to obtain the water vapor density and CO_2 density. Turbulent Kinetic Energy (TKE) derived from ECOR measurements are available in ARM EPCAPE Doppler Lidar profile statistics (DLPROFWSTATS: Newsom et al., 2025), is utilized here to understand the boundary layer turbulence. Lastly, the analysis is complemented with high-resolution vertical profiles of temperature, humidity, wind speed, and wind direction collected from radiosondes launched at Scripps Pier (Keeler, 2025). During April through September 2023, radiosondes were launched at 6-hour intervals (6 AM, 12 AM, 6 PM, and 12 PM). For the rest of EPCAPE, launches typically occurred twice daily at 12-hour intervals (6 AM and 6 PM).

2.2. SatCORPS GOES-18 satellite cloud products

Satellite retrievals are derived from the GOES-18's Advanced Baseline Imager (ABI) using a family of algorithms referred to as the Satellite Cloud and Radiation Property Retrieval System (SatCORPS). These algorithms are adapted from those developed by the Clouds and Earth's Radiant Energy System (CERES) to ingest radiances from geostationary sensors (Minnis et al., 2008, 2011, and 2023). For this study, the native resolution pixel retrievals at ~ 2 km are produced half hourly and gridded to 0.20˚x0.20˚ grid over the EPCAPE domain, defined here as the region covering the box of 28°N-43°N and 112.5°W-130°W. These gridded data are averaged according

https://doi.org/10.5194/egusphere-2026-933
Preprint. Discussion started: 6 March 2026

to their cloud height into low (height < 2 km), middle (2 km< height < 6 km), and high (height > 6 km) clouds. The cloud products include cloud fraction (CF), cloud optical depth, droplet effective radius, LWP, temperature, and height. Given the large uncertainties and limitations of optical retrievals during nighttime (optical depth and droplet effective radius) we only retain daytime observations with solar zenith angle (SZA) less than 70°. To minimize retrieval artifacts from thin or broken clouds, we apply additional screening criteria in our analysis: CF > 10%, $\tau > 2$ (Grosvenor et al., 2018). Also, we filter-out grid boxes with cloud top temperature (CTT) lower than 273.15 K and specifically select for this analysis averaged retrievals corresponding to the low height category (< 2 km) with LWP range of 5 – 250 g m^{-2} to limit the analysis to stratus and stratocumulus clouds and minimize retrieval uncertainties. The SatCORPS algorithm computes LWP using the relation:

$$LWP = (4/3) \cdot \rho_w \cdot \tau \cdot r_e / Q \qquad (1)$$

where ρ_w is the density of liquid water and Q is the cloud extinction efficiency, approximately 2.0. The cloud droplet number concentration (N_d) is estimated following the approximation for subtropical clouds in Painemal and Zuidema (2011) based on the adiabatic approximation:

$$N_d = 1.4067 \times 10^{-6}\ [\mathrm{cm}^{-1/2}] \cdot \tau^{1/2} / r_e^{5/2} \qquad (2)$$

Since numerous studies have reported a systematic positive bias in r_e derived from geostationary and sun-synchronous imagers of about 20% relative to in-situ data (e.g. Minnis et al., 2021; Painemal et al., 2023; Painemal et al., 2025), we apply a 0.8 correction factor to the r_e values before computing N_d, to minimize error propagations in Eq. (2). Consistency between the modified SatCORPS GOES-18 N_d and its ground-based counterpart (Section 3.5) validates this approach.

2.4. Self-Organizing Maps for synoptic regime classification

Self-Organizing Maps (SOMs; Kohonen, 1982; Kohonen, 1990; Bishop, 1995; Vesanto and Alhoniemi, 2000; Kohonen, 2001; Haykin, 2009) is an unsupervised machine learning technique designed to cluster and visualize high-dimensional data by projecting it onto a two-dimensional grid while preserving the topological relationships inherent in the data. The SOM algorithm groups similar data patterns into neighboring neurons on the grid, with each neuron i represented by a weight vector w_i. This weight vector is iteratively adjusted during training to reflect the distribution of the input data, ensuring that patterns with similar features are positioned

https://doi.org/10.5194/egusphere-2026-933
Preprint. Discussion started: 6 March 2026

close to each other on the grid. Recent studies emphasize the effectiveness of SOMs in synoptic climatology and environmental analysis (Hewitson and Crane, 2002; Sheridan and Lee, 2011; Jiang et al., 2013; Pearce et al., 2014; Juliano and Lebo, 2020; Painemal et al., 2023). The training process of SOMs involves several steps as described in Haykin (1999, 2009):

(1) Initialization: The weighting vectors of the neurons are initialized randomly for better convergence. Each neuron in the map is represented by a weighting vector with the same dimensionality as the input data.

(2) Determine the winning neuron i: For each input vector x, the algorithm calculates the Euclidean distance between the input vector and each neuron's weight vector. The neuron with the smallest distance to the input is selected as the winner, $\arg_i \min\|x-w_i\|$, where w_i represents the weight vector of the i^{th} neuron.

(3) Adapting weights: The winner and its neighboring neurons are updated to move closer to the input vector. The weight update for a neuron i at time t is given by:

$$w_i(t+1)=w_i(t)+\eta(t)h(i)(x-w_i(t));$$

where $\eta(t)$ is the learning rate which typically decreases over time and h(i) is the Gaussian neighborhood function, which determines how much a neuron is influenced based on its distance from the winner.

(4) Decay of Learning Rate and Neighborhood: Both the learning rate $\eta(t)$ and the neighborhood radius $\sigma(t)$ decrease over time to allow fine-tuning in later training stages: $\eta(t)=\eta0\ e^{-kt}$, $\sigma(t)=\sigma0\ e^{-kt}$; where $\eta0$ and $\sigma0$ are the initial learning rate and neighborhood radius, and k is a time constant controlling the decay rate.

(5) Iteration: This process is repeated over multiple epochs, iterating through the dataset either sequentially or in batches. Early epochs focus on global organization with larger neighborhoods and higher learning rates, while later epochs fine-tune the local structure, resulting in a topologically ordered map where similar input patterns are mapped to nearby neurons, allowing for the visualization and clustering of complex datasets.

https://doi.org/10.5194/egusphere-2026-933
Preprint. Discussion started: 6 March 2026

We utilized MiniSOM (Vettigli, 2018), a Python based implementation of SOM, which leverages the NumPy framework for computational efficiency, making it particularly suitable for analyzing moderate-sized datasets with minimal dependencies.

3. Results

3.1. Regional-scale classification

The first step in the synoptic clustering is to select the meteorological fields that will be used for the pattern classification. To this end, we consider a variable that represents the large-scale features over the region of study and a second parameter that captures local features along the coast. The clear choice that satisfies these conditions over the coastal NE Pacific are, respectively, sea level pressure (SLP, e.g., Juliano and Lebo, 2020) and boundary-layer wind fields at 975 hPa (e.g., Abel and Hall, 2010). We also experimented with adding the 500 hPa geopotential and winds at 850 hPa to SOM, which resulted in negligible changes in the clustering (not shown). Next, 11 years (2012-2022) of daily SLP and winds are normalized by subtracting the 30-day moving average at each 0.25° grid point and divided by the 30-day running standard deviation. This normalization ensures that the algorithm primarily discerns meaningful meteorological patterns rather than seasonal changes and extreme modes of variability. Alternative anomaly normalizations, such as spatial averaging methods used in previous studies (e.g., Juliano and Lebo, 2020), were tested but were found to disproportionately weigh land-ocean differences in SLP variability. As previously mentioned, we focus on the April through October, 2023 period, when the amount of low cloud cover peaks over the coastal northeast Pacific (e.g. Iacobellis and Cayan, 2013).

To determine the spatial domain extent best suited for capturing meteorological variability relevant to the NE California coast, we tested three domains of varying sizes: a large domain (10°N–50°N, 160°W–100°W), a medium-size domain (20°N–50°N, 140°W–110°W), and a small domain (30°N–40°N, 125°W–115°W). We found that the clustering for the large domain was dominated by large-scale changes in SLP far offshore, showing modest differences in meteorological conditions for the coastal region near Scripps Pier. In contrast, the small domain captured many more details that tended to yield spatially noisy patterns that lacked consistent features. The medium-sized domain (30° × 30°) provided the most representative patterns for the Southern California region, effectively capturing the dominant synoptic-scale features. We tested several objective methods to determine the optimal number of SOM nodes. First, we used the silhouette score to evaluate the uniqueness of patterns across different node selections. The score ranged from 0.065 for six clusters to 0.021 for nine clusters, degrading further with higher node counts, which rendered this method unsuitable. Second, we applied a two-step clustering approach: initially generating a larger SOM grid with 20 clusters (4 × 5 nodes) and then reclustering with K-means to reduce the number of patterns. However, this approach produced slightly noisier and less coherent patterns. Ultimately, the optimal number of nodes was chosen visually by testing several configurations (4 × 5, 4 × 4, 3 × 4, 3 × 3, etc.) to ensure clear classification of regional synoptic features. A 3 × 3 SOM (nine nodes) provided distinct, coherent synoptic regimes, striking a balance between capturing variability and maintaining interpretability. Moreover, this 3x3 SOM configuration effectively captures the evolution of the SLP discerned by the 4x5 SOM, as corroborated by comparing the normalized sea level pressure fields in Fig.1 and Fig S1.

The 9 synoptic patterns (regimes) determined by the SOM classification are depicted in terms of normalized SLP and 975-hPa winds in Fig. 1, with Scripp Pier represented by the yellow circle. The pattern shows a coherent evolution of SLP with distinctive differences across patterns. The most salient characteristics of the normalized fields are described as follows:

Pattern 1 is characterized by a strong anticyclone, with positive normalized SLP centered south of the Scripps Pier, a cyclonic feature farther north, and dominant offshore normalized winds. Pattern 2 depicts a diminished anticyclonic signature, with the cyclonic center shifting further south relative to pattern 1, and modest winds near the Pier. Pattern 3 displays the strongest normalized cyclone centered directly west of Southern California, producing broad onshore winds across the region.

Pattern 4 features an anticyclone strengthening with its center slightly north of Scripps Pier, and with intensified offshore flow. Pattern 5 presents minimal changes in SLP and winds and, thus, represents climatological features. Pattern 6 illustrates a moderate low-pressure system covering much of the domain, accompanied by enhanced onshore flow. Pattern 7 is the strongest high-pressure regime, with pronounced (normalized) offshore winds, and occurring 14.34% of the time (the highest frequency among all nodes). Pattern 8 is a transitional regime that shows a northward-displaced anticyclone and development of a modest low-pressure feature over Southern California. Lastly, pattern 9 depicts an additional northward displacement of the anticyclone, while the cyclone is centered near the Pier, generating strong (normalized) onshore winds.

It is interesting to observe a coherent transition of the anticyclone-cyclone system that resembles the evolution of weather disturbances, reflected in this clockwise order of clusters: 4, 1, 2, 3, 6, 9, 8, and 7. This SOM-based pattern classification serves as a foundational framework for identifying the dominant synoptic regimes during April to October, 2023 EPCAPE campaign period. By linking large-scale meteorological patterns to observed cloud and aerosol variability at the coast, this classification provides a valuable basis for understanding the meteorological processes that control the marine boundary layer evolution across the Southern California.

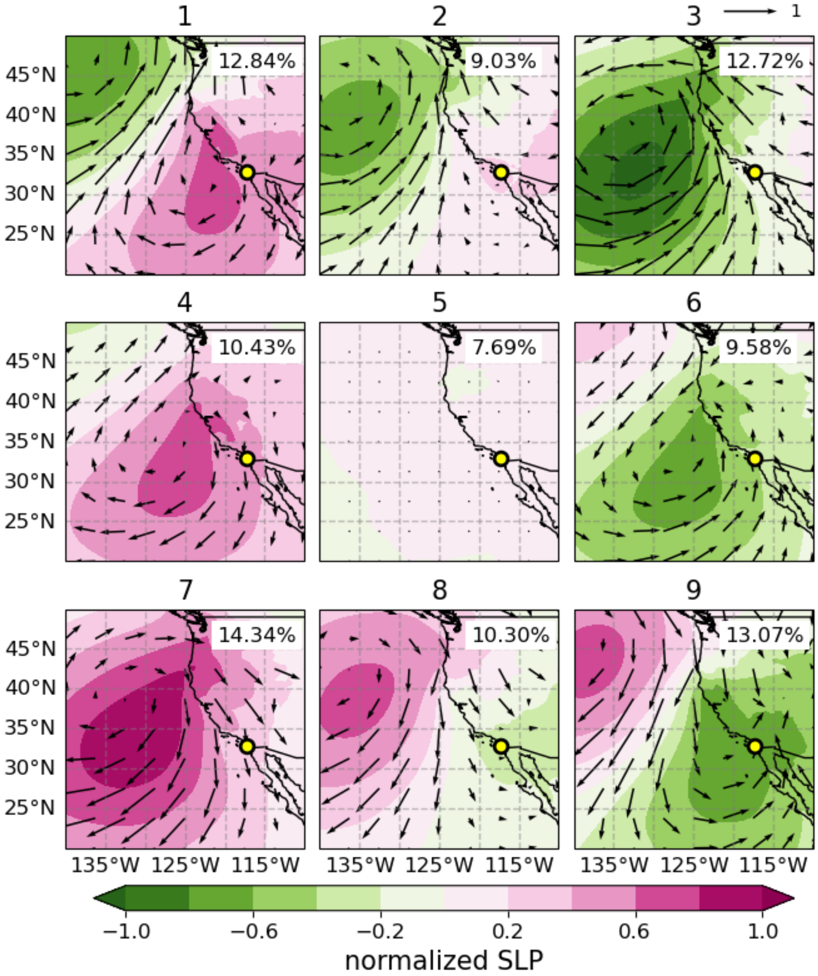

Figure 1: 11-year daily mean composite maps of normalized SLP and 975-hPa wind fields for the 9 regimes determined from SOM. Clusters are labelled from 1 to 9, and their frequency of occurrence is listed in percentage on the upper-right corner of each map. The yellow circle represents the location of the EPCAPE main site Scripps Pier.

3.2 General features of the synoptic regimes

We use SLP and wind fields in the boundary layer (975 hPa, ~ 300 m a.s.l.) and the free troposphere (750 hPa, ~ 2.5 km a.s.l.) for describing the circulation and transport pathways particularly for warm seasons. Table S1 summarizes the occurrence of the 9 regimes during the period of study. In addition, low-cloud control variables examined here include vertical velocity in pressure coordinates at 500 hPa, 750 hPa relative humidity, and lower tropospheric stability (LTS), defined as the difference in potential temperature (θ) between 750 hPa and the surface (similar to Klein and Hartmann, 1993). The meteorological fields for each regime are depicted as mean composites in Fig. 2, and as anomalies relative to the monthly running mean in Fig. 3. While the discussion is mainly guided by Fig. 2, Fig. 3 provides quantitative information of magnitude changes of the deseasonalized fields. The SLP patterns in Fig. 2 features a dominant anticyclone with varying values of magnitude and extent anticipated by Fig. 1. Regime 3 captures the weakest anticyclone and confined to the south of the EPCAPE site, a weak cyclonic region over the northern area, and relatively weak winds (<5 m/s) in the boundary layer. In contrast, Regime 7 depicts the strongest development of the anticyclone, with boundary layer winds exceeding 10 m/s near the Scripps Pier. Similarly, the high-pressure system is well developed in regimes 8 and 9, but with their core displaced farther northwest than in regime 7, and with wind speeds greater than 10 m/s. Regimes 7, 8, and 9 feature wide areas of subsidence (positive pressure velocity, solid black contours) and consistent free tropospheric drying over the ocean. For these regimes with intense mean and deseasonalized anticyclone, we observe a strengthening of the coastal winds parallel to the coast south of 40˚N. Notably, these coastal winds tends to be stronger in the boundary layer (Fig 2a, arrows) than in the lower free troposphere (Fig. 2b, arrows), which is a common feature of the coastal low-level jet around Cape Mendocino (40.4˚N, Parish, 2000). Regimes 1, 2, and 3 are unique in that they feature a weak cyclonic circulation north of 40˚N, with westerly winds north of 35ºN, and concomitant with 500 hPa ascents (Fig 2a, black dashed contours). Regime 4 shows a moderately developed anticyclone but with relatively modest deseasonalized values (Fig 3a), with its center aligned with the latitude of Scripps Pier. Regime 5 features the climatological mean pattern, as discussed in Section 3.1.

In terms of 750 hPa winds, consistent with the strengthening of the anticyclonic and cyclonic circulation, regimes 1–3 exhibit a dominant zonal component, suggesting transport of marine air masses inland. For 7–9 (anticyclones), winds run parallel to the coast, potentially contributing with a mixture of continental and marine air masses to Scripps Pier. For regimes 4–6, the wind direction shows intermediate transitions between 1–3 and 7–9. While there is an increase in LTS for all the regimes for the broad coastal area south of 40˚, regimes 5, 6, and 8 feature the highest values (>20 K). It is, nevertheless, surprising that deseasonalized anomalies in Fig. 3b show modest variability for the same coastal area, especially near Scripps Pier, with interregimes differences smaller than 3 K, and with unclear connections with the atmospheric circulation depicted in Fig. 3a. This implies that the patterns of the mean LTS in Fig. 2b primarily reflect seasonal changes rather than synoptic-scale processes. As we will see in the following sections, the modest variability in LTS cannot explain changes in the cloud fields, confirming the poor correlation between LTS and cloud cover at synoptic scales reported by a number of studies (e.g. Klein et al., 1997).

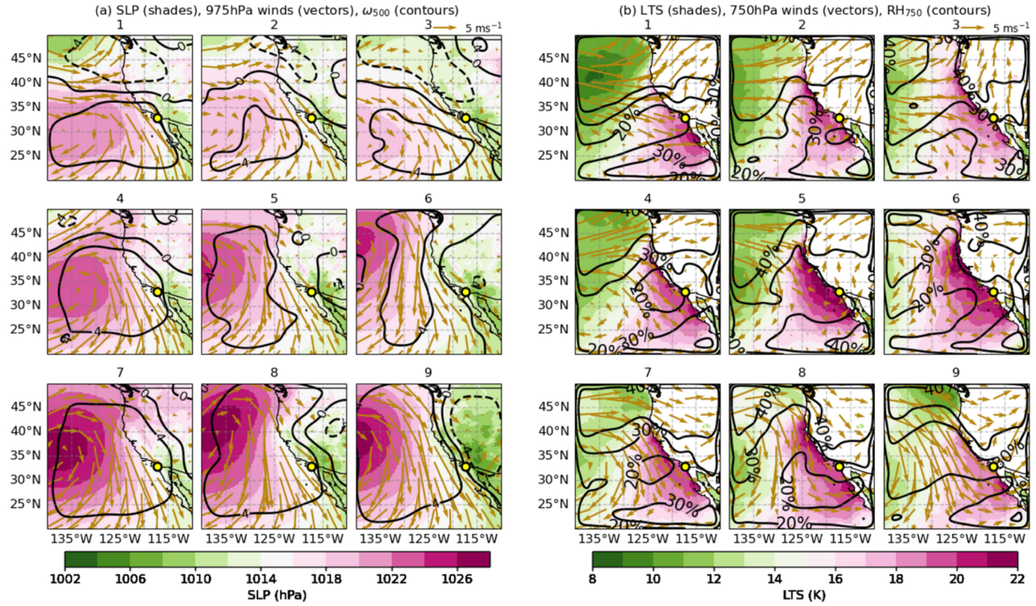

Figure 2. Composite maps of mean meteorological fields for the nine synoptic regimes identified for the April – October 2023 during the EPCAPE campaign. (a) Sea level pressure (SLP; color shading), 975 hPa winds (vectors), and pressure vertical velocity at 500 hPa (x 10^{-2} Pa/s; black contours). (b) Lower tropospheric stability (LTS; shading), 750 hPa winds (vectors), and relative humidity at 750 hPa (RH_{750}; black contours).

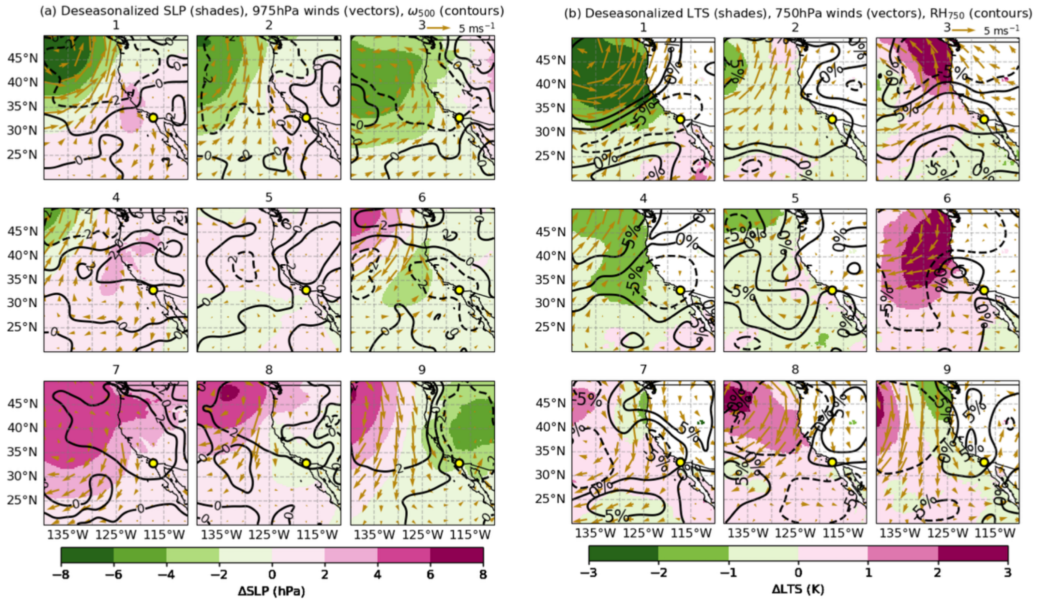

Figure 3. Deseasonalized meteorological field (using the 30-day running mean) for the nine synoptic regimes identified for April through October 2023 during the EPCAPE campaign. (a) Sea level pressure (SLP; color shading), 975 hPa winds (vectors), and pressure vertical velocity at 500 hPa (x 10^{-2} Pa/s; black contours). (b) Lower tropospheric stability (LTS; shading), 750 hPa winds (vectors), and relative humidity (RH) at 750 hPa (RH_{750}; black contours).

3.3 Atmospheric structure derived from Radiosonde observations at Scripps Pier across nine synoptic regimes

After providing a regional description of the atmospheric variability over the coastal NE Pacific, we center our attention on the thermodynamical properties of the lower troposphere derived from radiosondes observations collected during EPCAPE at Scripps Pier. Figures 4 and 5 provide, respectively, median and deseasonalized atmospheric profiles for each regime. The boundary layer for all regimes is statically stable, with mean values ranging between 17 – 20 K (Fig 4a). Regime specific features are more easily observed in the θ anomaly (deseasonalized) profiles in Figure 5a. Regimes experiencing intense anticyclonic circulation (e.g., regimes 8, 9) depict negative θ anomalies (about –2 K) and less stable conditions, while the other regimes generally show positive θ anomalies, which exceed +4 K for regime 3 and 6. In terms of relative humidity, most regimes maintain high RH (>80%) in the boundary layer with the expected sharp decrease in the free troposphere (Fig 4b). Median RH profiles suggest shallow MBL tops (0.5–0.8 km) in most regimes, while regimes 8 and 9 feature deeper and moister layers extending beyond 1 km. These regimes are associated with synoptic conditions that promote upward moisture transport, particularly regime 9, which maintains elevated RH throughout the lowest 2 km, consistent with moist northwesterly flow and enhanced ascent (Zhou et al., 2015). In addition, stronger boundary-layer turbulence from intensified winds, together with enhanced entrainment under relatively weaker static stability, likely contribute to the boundary-layer deepening observed in regimes 8 and 9. Consistently, RH anomalies in Fig 5b show that regimes 8 and 9 exhibit large RH positive anomalies (10–20%), while regimes 3 and 6 show persistent negative anomalies revealing relatively dry boundary layer. Regimes 1, 4, and 7— typically associated with anomalous high-pressure and subsidence in coastal regions — exhibit negative RH anomalies (-10%).

Wind profiles in Fig 4b and c generally feature modest zonal wind speeds (U) (~2 m s^{-1}) within the boundary layer. Regimes 7, 8, and 9 – dominant under high-pressure influence – exhibit moderate westerlies that increase with height in the free troposphere. Meridional wind (V) profiles are more revealing of the position and strength of the anticyclone: Most regimes are dominated by a modest but persistent northerly flow (negative V), consistent with cold air advection and coastal subsidence typical of summertime marine stratus regimes (Parish et al., 2000). On the other hand, regime 9 displays southerly flow (positive V), indicative of warm, moist advection into the coastal boundary layer, enhancing cloud development and aerosol transport from offshore (Painemal et al., 2013a). In regime 9, meridional winds are as strong as 2 m s^{-1} within the BL, dominating the horizontal wind structure and suggesting onshore transport.

https://doi.org/10.5194/egusphere-2026-933
Preprint. Discussion started: 6 March 2026

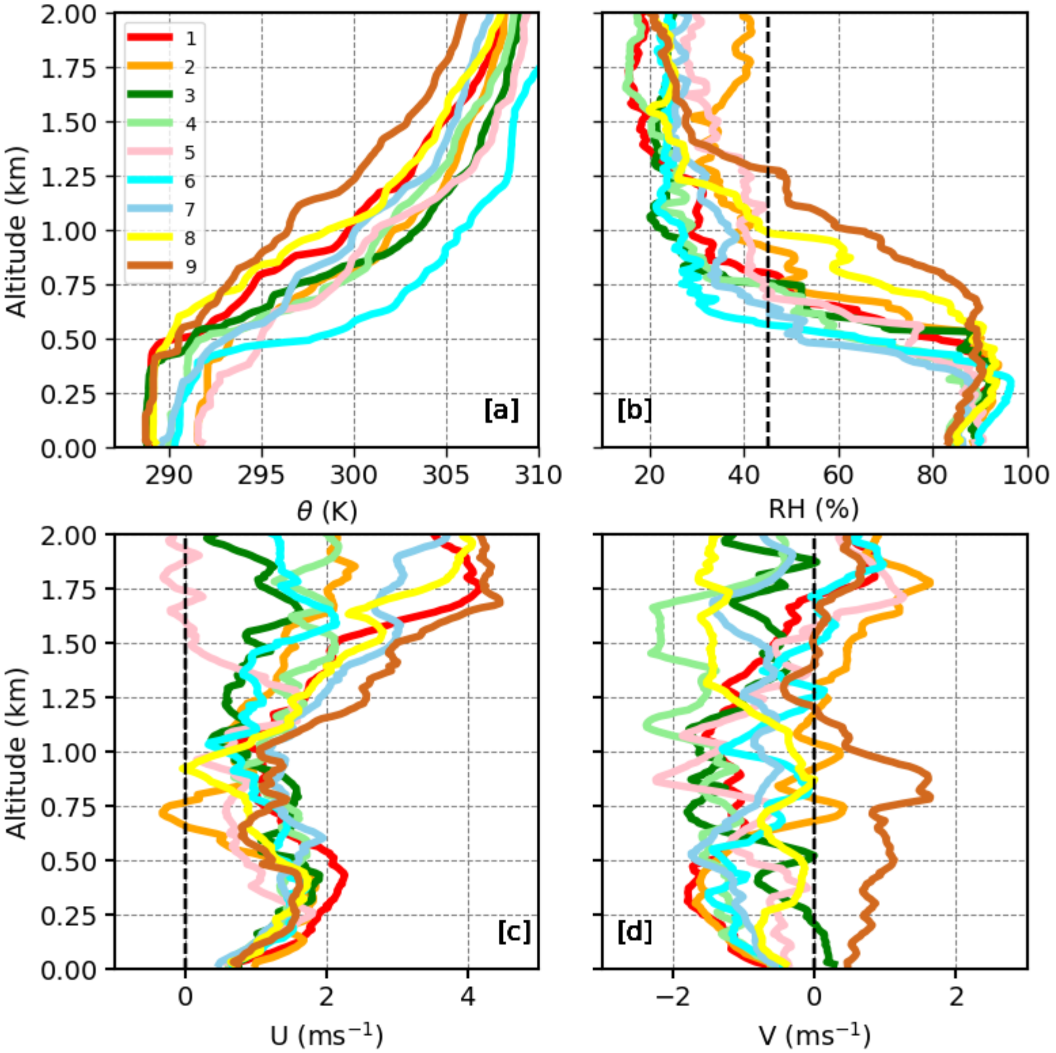

Figure 4. Regime-composite median vertical profiles of thermodynamic variables for the lowest 2 km from radiosonde observations for April to October 2023 during EPCAPE, for the nine synoptic regimes. (a) potential temperature (θ), (b) relative humidity (RH), (c) zonal wind (U), and (d) meridional wind (V). Daily 6am and 6pm profiles are included. Vertical dashed line in (b) indicate 45% RH threshold depicting BLH.

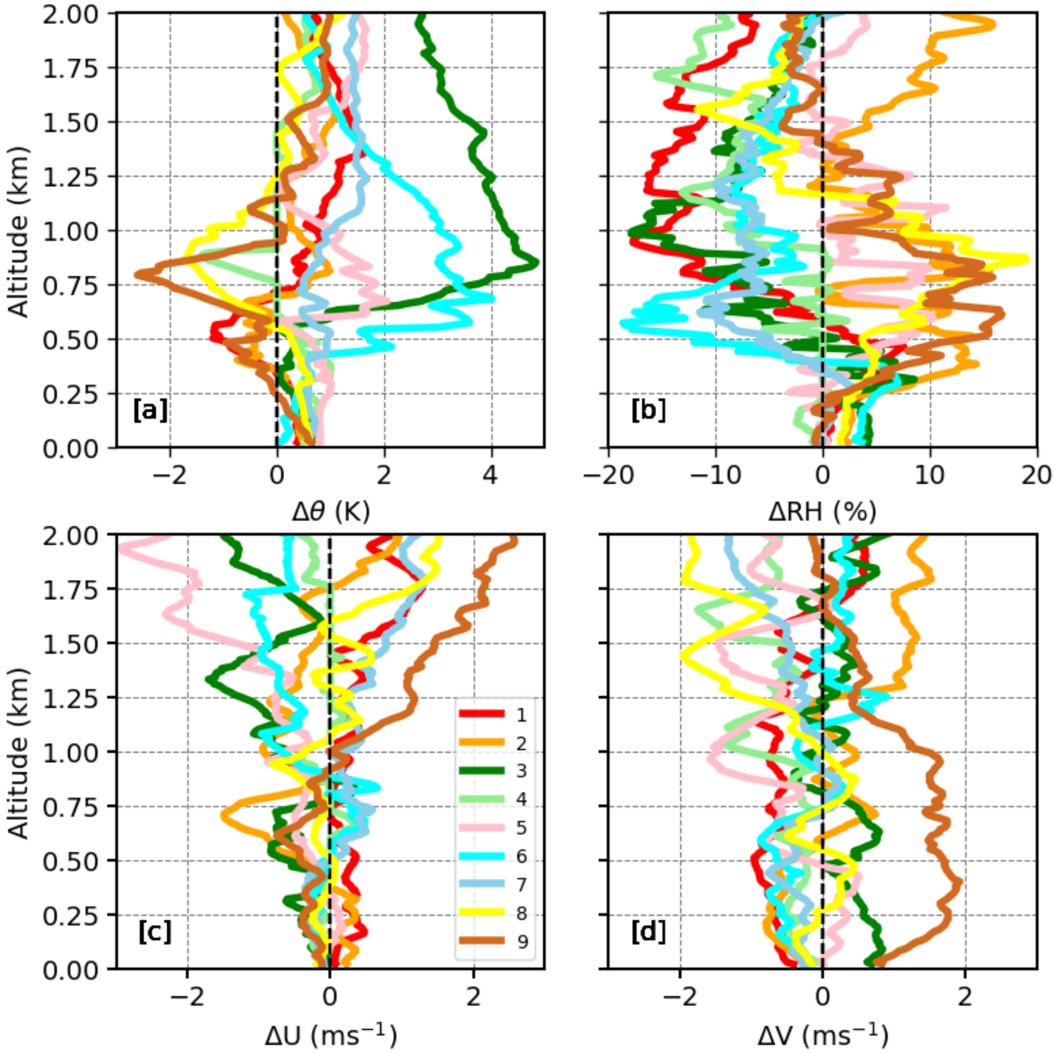

Figure 5. Regime-based median profiles of the deseasonalized thermodynamic variables for the lowest 2 km for April to October 2023 during EPCAPE, computed as deviations from the 30-day running mean. (a) Potential temperature anomaly (Δθ), (b) relative humidity anomaly (ΔRH), (c) zonal wind anomaly (ΔU), and (d) meridional wind anomaly (ΔV). Dashed vertical lines represent the zero-anomaly reference.

https://doi.org/10.5194/egusphere-2026-933
Preprint. Discussion started: 6 March 2026

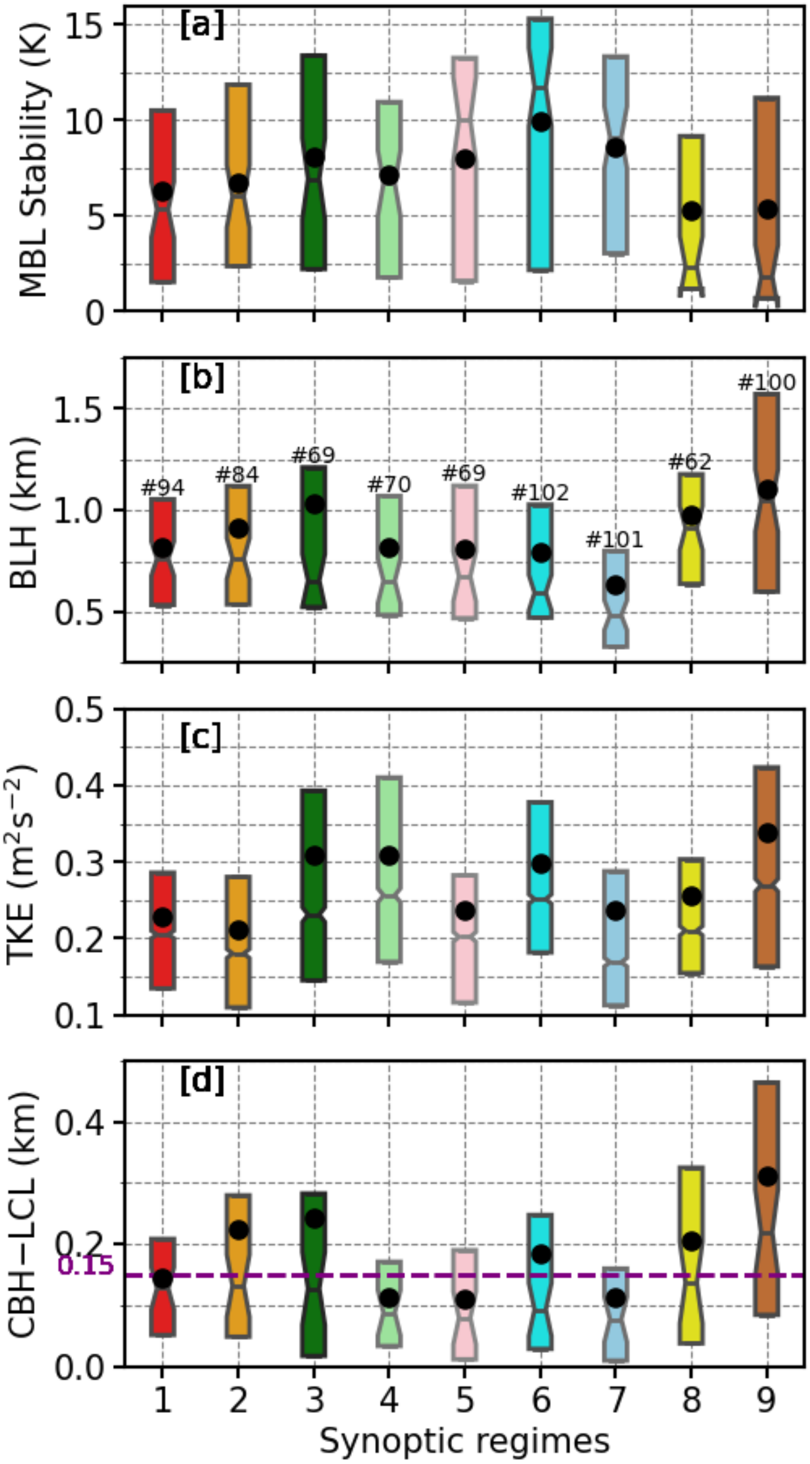

454

Figure 6: Boxplot of (a) MBL stability metric, (b) boundary layer height (BLH), (c) turbulent kinetic energy (TKE), and (d) CBH – LCL difference, for the nine synoptic regimes for April through October 2023 during EPCAPE at Scripps Pier. Boxes show interquartile range with medians marked by horizontal lines, and black circles denote the mean. *Notches represent the 95% confidence interval of the median, according to the test described in* Krzywinski and Altman, (2014). The magenta dashed line in (d) marks the 150 m threshold used in Jones et al. (2011) to identify decoupled boundary layers. *The number of samples for each regime is shown on the figure panel (b).*

Specific properties that characterize the boundary layer are presented in Fig. 6. Boundary-layer stability is quantified from radiosonde observations using a MBL stability metric, defined as the potential temperature difference between 700 m and the surface. Regime-mean values range from 5 to 10 K, with larger values indicating a more stable MBL and smaller values reflecting enhanced turbulence. Regime 6 shows the highest values, consistent with the most stable conditions and a stronger inversion. Such thermodynamic conditions tend to favor shallow, persistent stratocumulus clouds with limited vertical development (Teixeira et al., 2011; Zhou et al., 2015). Conversely, regimes 8 and 9 show lowest stability metric values, suggesting stronger MBL turbulence. The boundary layer height (BLH) is simply estimated as the altitude for which RH drops below 45 % (Bretherton et al. 2010). BLH exhibits moderate variability across regimes (Fig 6b). Regime 7 has the lowest median BLH (~750 m), consistent with its association with strong subsidence that inhibits vertical development of the MBL. In contrast, regimes 8 and 9 display a deeper boundary layer. Deeper MBL is typically conducive to enhanced vertical cloud extent and increased LWP, a trend consistent with the regime-specific cloud structures to be discussed in Sections 3.4 and 3.5.

Figure 6c shows the distribution of TKE across the nine SOM synoptic regimes, highlighting substantial regime-dependent modulation of boundary-layer turbulence. Regimes 3, 4, 6, and 9 exhibit the largest mean TKE (around 0.3–0.35 $m^2 s^{-2}$) and broad upper quartile ranges, favoring of strong turbulent mixing of the boundary layer. In contrast, regimes 1, 2, 5, and 7 show lower mean TKE (around 0.20–0.25 $m^2 s^{-2}$) and narrower distributions, representing a weakly turbulent boundary layer. Notably, regime 2, exhibits the lowest TKE values. Lastly, regime 8 depicts moderate mean TKE, which is also regime with deeper and a weakly stratified BL.

https://doi.org/10.5194/egusphere-2026-933
Preprint. Discussion started: 6 March 2026

The difference between cloud base height (CBH) and the lifting condensation level (LCL) provides insight into the degree of cloud-boundary layer coupling (Fig 6d). A CBH–LCL separation exceeding approximately 150 m (highlighted by the dashed line) typically signifies decoupled conditions, wherein the cloud layers are no longer directly connected to the surface moisture supply and below-cloud turbulence (Wood and Bretherton, 2004; Jones et al., 2011). Regimes 2, 3, 6, 8, and 9 frequently exhibit upper quartiles with CBH–LCL values that exceed the 150-m threshold, with the highest mean and median for regime 9, indicating frequent decoupling. Conversely, regimes 1, 4, 5, and 7 maintain tightly clustered CBH–LCL distributions near or below 150 m, indicative of well-coupled marine boundary layers. In such regimes, cloud bases closely follow the lifting condensation level, enhancing aerosol–cloud interactions and generally supporting higher cloud droplet number concentrations as discussed in the section 3.6, assuming sufficient aerosol availability (Wood, 2012).

3.4 Cloud characteristics for synoptic regimes

To characterize the link between synoptic-scale meteorology and low-level clouds along the Southern California coast during the EPCAPE, we create regime composites of SatCORPS GOES-18 cloud properties. Figure 7 presents the spatial mean distributions of key low-level cloud properties: low-level cloud fraction (LCF), N_d, LWP, and CTH. Figure 8 shows the corresponding spatial anomalies of these variables, calculated relative to the 30-day running mean climatology. Figs. 7a and 8a show that low-level clouds are less frequent when the subtropical anticyclone center is closer to the coastal Southern California (regimes 1, 2, 4, 5, 7). In these regimes, the fractional low-cloud amount is below 50% along the coastline and increased to 70 – 80% over the southern offshore domain. The considerable mid+high cloud incidence (>50 %, Fig. S2) in this regimes indicates that the corresponding low-cloud reduction is partially attributed to obscuration of higher clouds in the satellite sensor field of view. Notably, Regime 3 is primarily linked to synoptic storm systems in midlatitudes, indicating that deeper convection and frontal systems play a dominant role in shaping the clouds in this regime. In contrast, regimes characterized by an offshore high pressure and a developing low pressure over land (regimes 6, 8, and 9) display greater low cloud amount exceeding 70% along the southern California shoreline and offshore. Indeed, the positive deseasonalized anomalies in LCF reach up to +20% in these regimes and this increase in low-cloud coverage is consistent with wide regions with subsidence and a reinforcement of the northerly winds (Fig 2a), two factors that favor the strengthening of the thermal inversion (Myers and Norris, 2013; Wood, 2012). Regime 5, the regime closest to climatological neutrality, displays average LCF values (~50%), but shows negative anomalies (~5 to 10%) around the EPCAPE site.

Figures 7b and 8b show the spatial mean and anomaly fields of SatCORPS GOES-18 N_d across the nine synoptic regimes. All regimes exhibit a strong coastal gradient in N_d with local maxima (>200 cm^{-3}) occurring nearshore and a systematically westward decrease. This well-known pattern is consistent with an expected continental aerosol outflow, dilution and precipitation scavenging offshore. Interestingly, under well-developed high-pressure conditions with stronger boundary layer winds (e.g., regimes 7 – 9), N_d enhancement is limited to a narrow coastal band and decreases abruptly to ~100 cm^{-3} offshore. This suggests that intense anticyclonic circulations hinder the transport of continental aerosol over the open ocean, confining CCN sources to coastal regions. In contrast, regime 6 features the largest extent of positive N_d anomalies and mean values greater than 175 cm^{-3}, associated with a northwest displacement of the anticyclone and winds that run parallel to the coast north of 35˚N. This unique synoptic configuration was also identified in Painemal et al. (2015) as the circulation that drives the highest N_d during MAGIC over the NE Pacific.

(a) Mean low cloud fraction

(b) Mean Cloud droplet number concentration

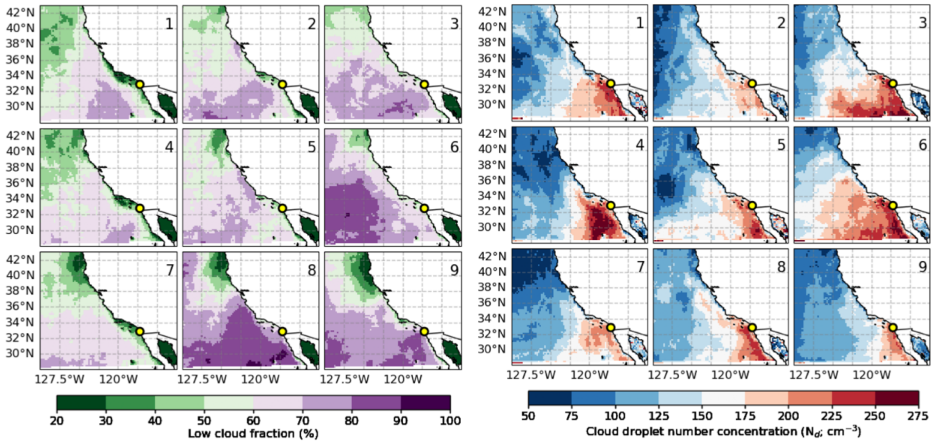

(c) Mean liquid water path

(d) Mean cloud top height

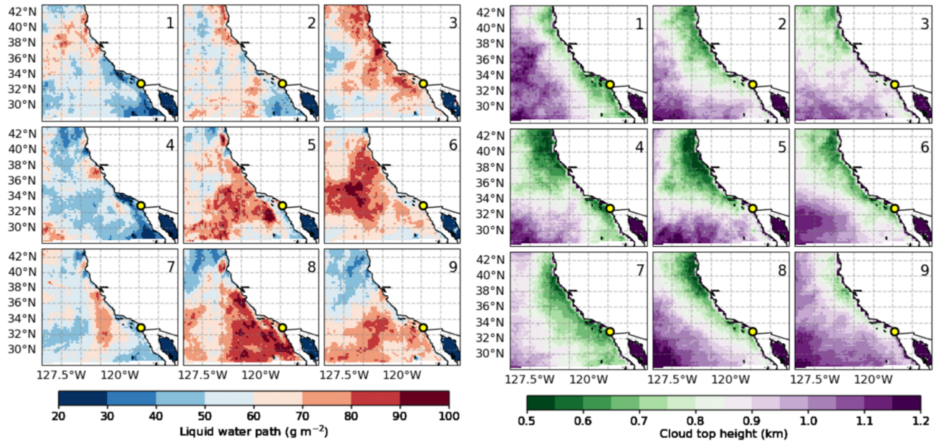

Figure 7: SatCORPS GOES-18 cloud properties composited across nine synoptic regimes for April to October 2023 during the EPCAPE period: (a) low-cloud fraction, (b) cloud droplet number concentration, (c) liquid water path, (d) cloud top height. The magenta circle indicates the Scripps Pier site.

In terms of LWP, the 9 regimes feature pronounced contrasts (Fig. 7c and 8c). Broadly, the locations of anomalous high-pressure areas relate well with the locations of lower LWP. In connection to this, regimes 1, 2, 4, and 7 – where the anomalous SLP is positive – display low LWPs with mean values typically below 50 g m^{-2}, and anomalies reaching as much as 25 g m^{-2} less than the mean climatology. These regimes are often characterized by shallower marine boundary layers with CTH below 800 m. Regimes 3, 6, 8, and 9 exhibits enhanced LWP frequently exceeding 75 g m^{-2} across large spatial extents. These regimes also show strong positive LWP anomalies, in some cases surpassing 25 g m^{-2} compared to climatological means. High values of LWP appear to be explained by 2 factors: a) ascents and potential convection in regime 3, b) and a boundary layer deepening (Fig 8d) for regimes 6 and 9. Regionally, SatCORPS CTH (Fig. 7d) shows shallower clouds along the coast, a region with cooler sea surface, with cloud top deepening farther offshore over warmer waters. Most synoptic regimes exhibit mean CTH values of ~600–800 m, except regimes 3, 5, and 9, which reach ~1 km. Notably, regime 3, the most prominent case influenced by a midlatitude cyclone, features the deepest coastal clouds. Deseasonalized CTH patterns highlight distinct variations: regimes 1, 4, 7, and 8 display systematically lower cloud tops, while regimes 3, 6, and 9 show higher cloud tops, particularly over the Southern California sector of the NEP. Anomalies in the remaining regimes are weak and generally within ±50 m.

https://doi.org/10.5194/egusphere-2026-933
Preprint. Discussion started: 6 March 2026

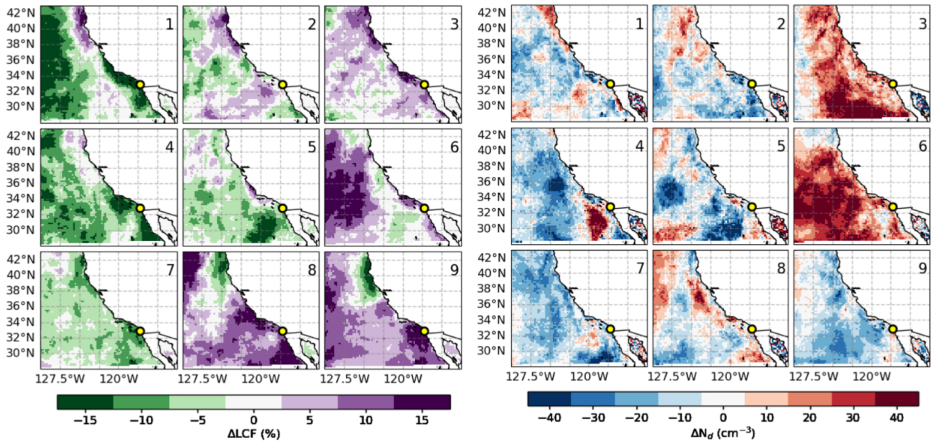
(a) Low cloud fraction anomaly

(b) Cloud droplet number concentration anomaly

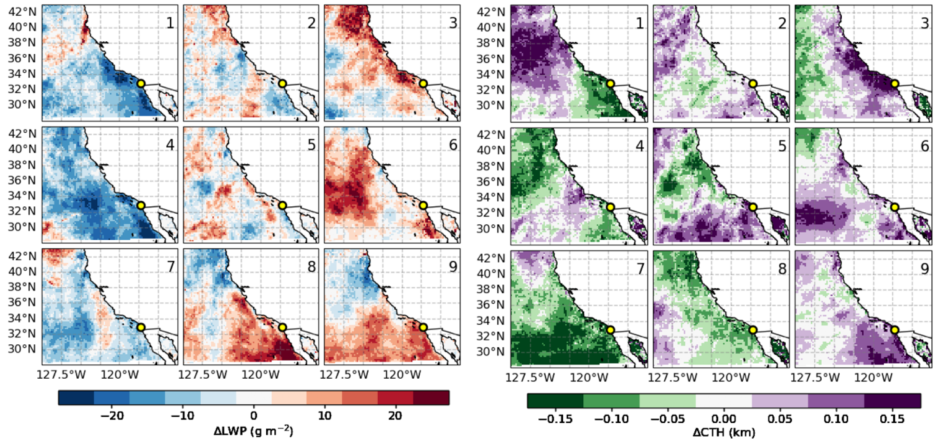
(c) Liquid water path anomaly

(d) Cloud top height anomaly

Figure 8: SatCORPS GOES-18 composite anomalies across nine synoptic regimes for April to October 2023 during the EPCAPE period: (a) low-cloud fraction, (b) cloud droplet number concentration, (c) liquid water path, (d) cloud top height. The magenta circle indicates the Scripps Pier site. Anomalies are computed relative to the 30-day running mean climatology.

3.5 Cloud characteristics from observations at Scripps Pier

Regime-specific comparison of SatCORPS satellite retrievals and EPCAPE ground-based observations of key cloud properties at Scripps Pier are shown in Fig. 9. The SatCORPS satellite data here correspond to the 0.2° grid box closest to Scripps Pier. Both GOES-18 and KAZR-derived CTHs exhibit similar variability across regimes and generally agrees within 100 m. A key difference is the smaller lower quartile magnitude for the KAZR, likely attributed to the ability of the radar to detect small shallow cumulus clouds that are undetected at the satellite pixel resolution. The KAZR CTH resolves the shallowest median cloud tops (<1000 m) in regimes 4 and 7, where the anticyclone is centered closer to Scripps Pier, as indicated by positive SLP anomalies over the pier and adjacent land areas, and in agreement with the ground-based radar CTH (Fig. 7d and 8d). In contrast, deeper cloud tops are observed in regimes with an anticyclone accompanied by a weak coastal low (regimes 8 and 9, Fig. 2a), reflected in negative anomalous SLP around Scripps Pier (Fig. 3a). The ceilometer-based CBH in Fig 9b shows that regime 6 often develops cloud bases closer to the surface (median ~ 250 m), under the most stable boundary layer conditions (Fig. 6a). The mean CBH is within 400 m in regimes with an anticyclone centered close to Scripps Pier (regimes 1, 4, and 7) and follows a decrease in CTH. The deviation of mean and median CBH in regime 2 and 3, reveals the likely influence of episodic passages of cyclonic system, contributing with samples featuring deep boundary layers. Regimes 8, and 9, on the other hand, show the highest mean cloud base (> 600 m) in accordance with more turbulent, deeper, and decoupled BL. Figure 9c shows LWP variation across regimes, generally with comparable interquartile ranges, though slightly larger values occur in regimes 1, 3, and 9.

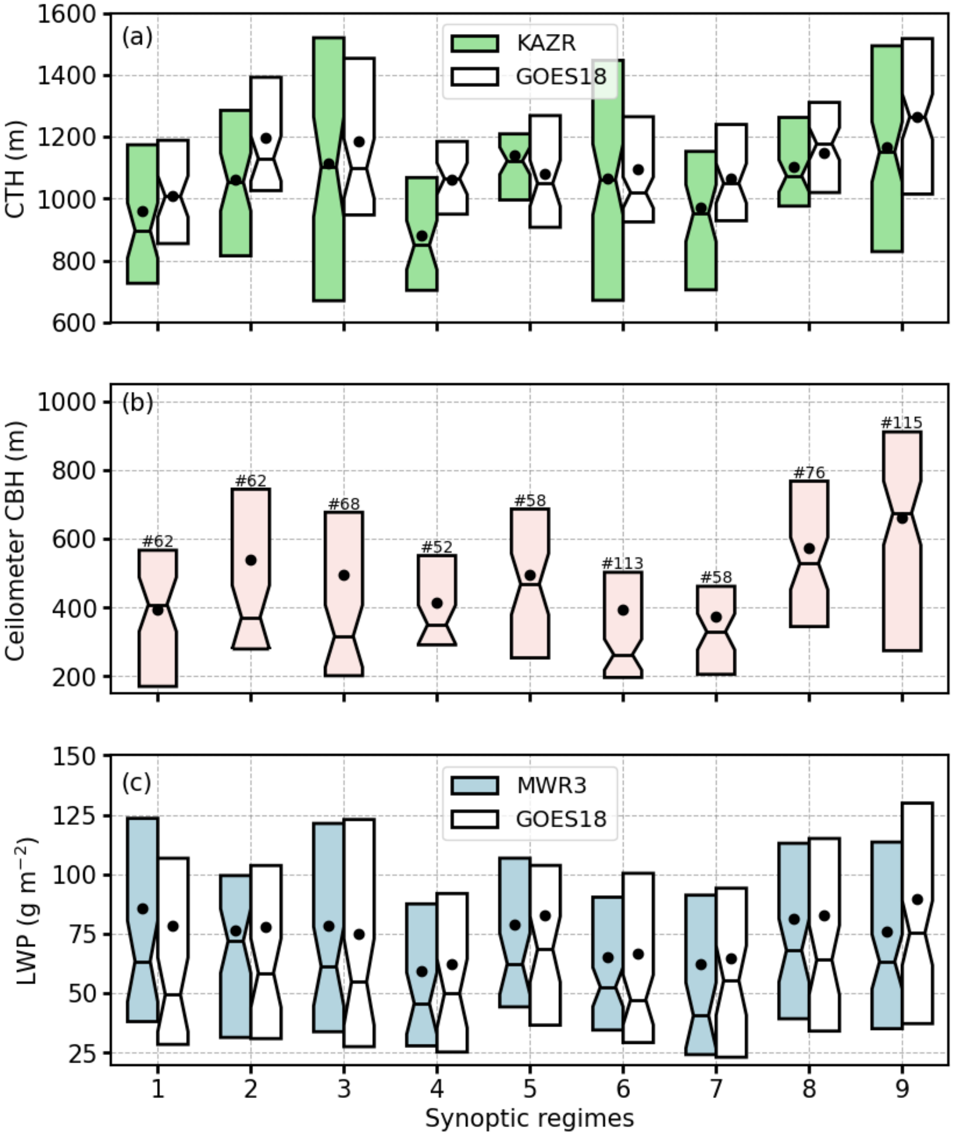

Figure 9: Comparisons of SatCORPS GOES-18 satellite vs. EPCAPE ground-based observations of (a) cloud top height, (b) cloud base height, and (c) liquid water path at Scripps Pier for April to October 2023 during EPCAPE. The criteria of ceilometer derived hourly cloud frequency fraction > 0.2 and SatCORPS GOES-18 low cloud fraction > 10 % is selected to identify the persistent stratiform clouds. *Notches represent the 95% confidence interval of the median. The number of samples for each regime is shown on the panel(b).*

3.6 Aerosol and cloud droplet concentration at Scripps Pier

To assess how synoptic regimes modulate aerosol variability and transport at Scripps Pier, we analyze number concentrations of smaller particles (Na ≤ 0.1 µm, $N_{a\leq0.1}$) and larger accumulation-mode particles (Na >0.1 µm, $N_{a>0.1}$), derived from merged SMPS and APS measurements (Fig 10a). Smaller particles are typically associated with fresh local emissions and pollution, whereas larger particles reflect aging-driven growth or contributions from marine and continental sources such as sea spray or dust. Both size modes exhibit substantial variability across synoptic regimes. As inferred from Fig. 10a, upper quartile concentrations of smaller-sized particles exceed 600 cm^{-3} for all the regimes, but with the lowest medians for regimes 3, 6, and 8. While larger-size particles generally follows a similar regime evolution, the lowest median values (<400 cm^{-3}) are confined to regimes 2, 8, and 9. Overall, $N_{a\leq0.1}$ are significantly higher than $N_{a>0.1}$ most regimes; however, regime 6 – characterized by a strong, stable boundary layer – shows comparable concentrations between the two size modes.

In terms of CCN at 0.2% of supersaturation ($CCN_{0.2\%}$, Fig. 10b, blue), regime changes are somewhat similar to $N_{a>0.1}$, with concentrations comparable to those for $N_{a\leq0.1}$. CCN at 0.1 % supersaturation ($CCN_{0.1\%}$) is, as expected, smaller than $CCN_{0.2\%}$ but with qualitatively similar regime changes. These changes in CCN with supersaturation can be analyzed in the context of clouds by examining variation in cloud droplet number concentration derived from GOES-18 and from the remote sensors at the pier (Fig. 10c). N_d values are similar to the concentrations for $CCN_{0.1\%}$, suggesting small magnitudes of supersaturations present in this region, limiting the number of particles activated despite relatively large aerosol concentrations (Fig. 10a). Both satellite and the ground-based remote sensors show similar changes in N_d with regimes, but with larger interquartile ranges for the ground-based observations. The discrepancies between ground-based and GOES-18 N_d cannot be easily explained as we do not count on independent in-situ observations to validate these computations. Therefore, the data interpretation will be based on features common to both satellite and ground-based N_d. Regime 2 consistently exhibits the lowest mean N_d (~150–200 cm^{-3}), whereas regimes 3 and 7 show the highest mean N_d (~300 cm^{-3}), and regimes 9 exhibits the highest upper quartile value. N_d for other regimes does not show meaningful changes. While aerosol loading is controlled by synoptic and local variability, N_d responses are likely influenced by BL turbulence and internal cloud dynamics.

For assessing the impact of turbulence in aerosol and cloud droplet concentration, we bin N_d as function of accumulation mode N_a and TKE bins (Fig. 12). As TKE increases from 0.1 to 0.5 m^2 s^{-2}, large-aerosol particle concentrations monotonically increase from 320 to 550 cm^{-3}, suggesting that enhanced turbulence promotes aerosol growth into accumulation mode aerosols. In addition, we observe an increase of the ground-based N_d with TKE, with changes that exceed 200 cm^{-3}. This underlines the role of turbulence in strengthening aerosol activation into CCN. The averaged N_d as a function of TKE and N_a indicates that an increase in N_a combined with strong TKE leads to a higher N_d. Interestingly, only for N_a >400 cm^{-3}, N_d increases with TKE to values greater than 250 cm^{-3}.

Backtrajectories in Fig 11 are dominated by a flow that runs parallel to the coast (Han et al., 2025; Maneenoi et al., 2025). A departure from this pattern is observed for regime 7, which features a significant number (~ 47%) of trajectories that originate from or intersect land areas. Given the modest changes in the backtrajectory pattern per regime, it is not possible to establish a relationship between long-range transport, backtrajectories, and aerosol variability. This suggests that for this coastal site, local aerosol sources and transport (e.g., land-sea breeze), are, at least, as important as the synoptic meteorology for explaining aerosol variability.

In terms of aerosol composition, non-refractive organics is the dominant species at Scripps Pier, followed by sulfate and ammonium (Fig 13). A synoptic-scale minimum in organics is identified for regime 9, accompanied with a minimum median in sulfate and ammonium. In contrast, regime 7 features a maximum median in organics, which is consistent with the regime that features the largest number of 48-h backtrajectories that transit over land (Fig. 11). For other regimes, changes in mass concentration are modest.

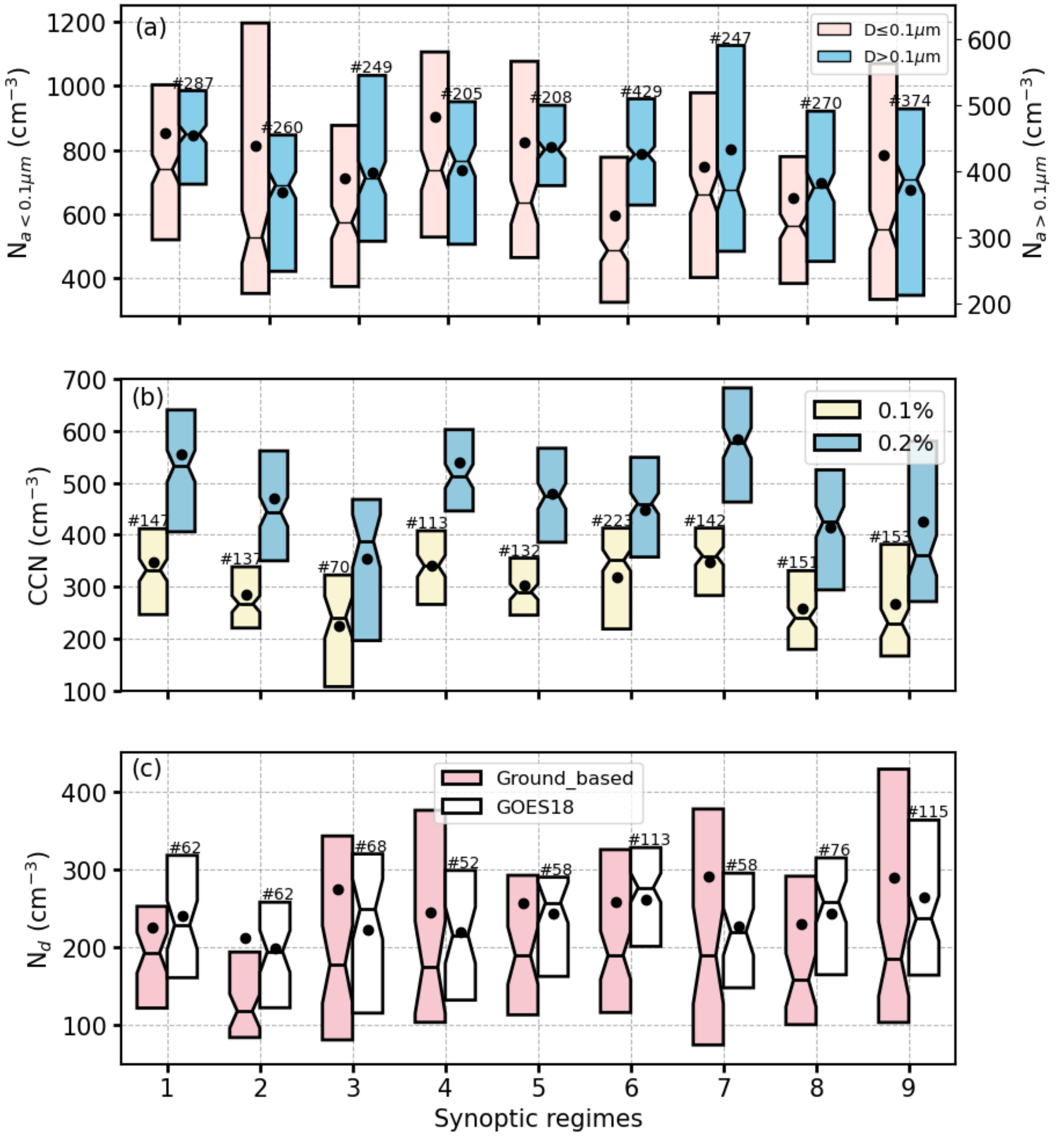

Figure 10: Boxplot of (a) aerosol number concentrations N_a (cm^{-3}), (b) cloud condensation nuclei (cm^{-3}), and (c) cloud droplet number concentration (cm^{-3}) for nine synoptic regimes at Scripps Pier for April to October 2023. *Notches represent the 95% confidence interval of the median. The number of samples for each regime is shown on the figure.*

https://doi.org/10.5194/egusphere-2026-933
Preprint. Discussion started: 6 March 2026

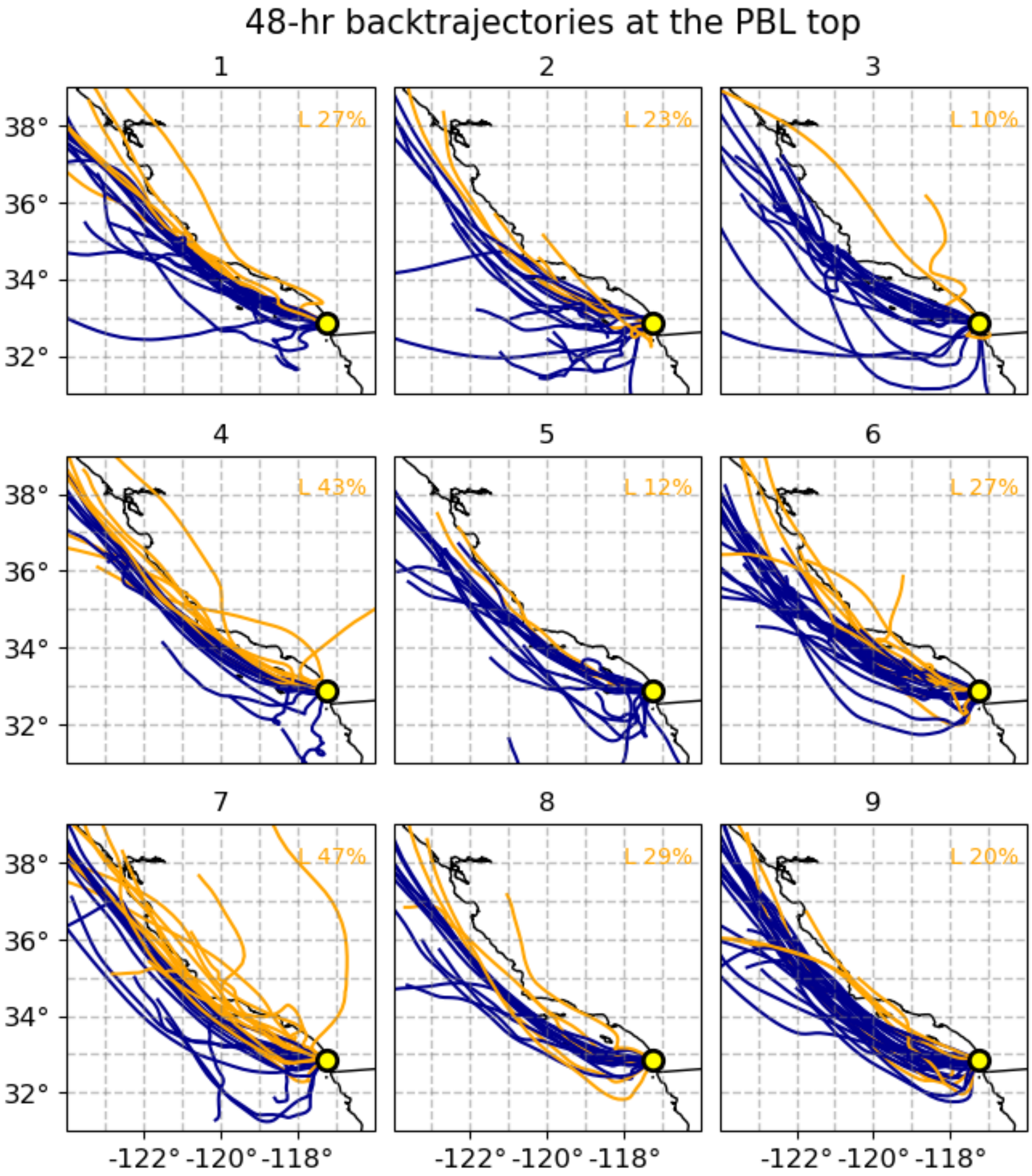

Figure 11: ARMTRAJ-PBL airmass backtrajectories initiated at Scripps Pier (yellow circle) at PBL top for the nine synoptic regimes labelled from 1 to 9. Trajectories from or crossed over land are shown in orange color, and the corresponding percentage of trajectories for each regime is shown on the figure.

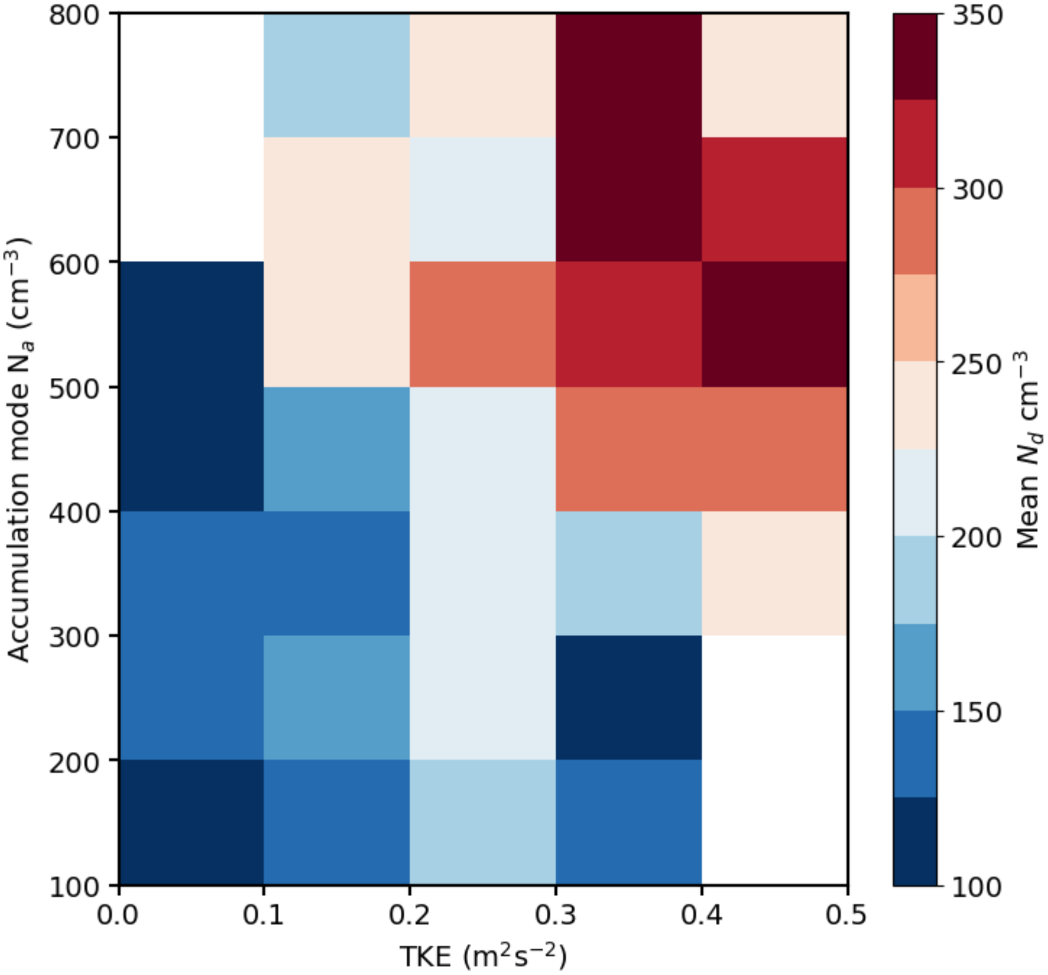

Figure 12: Relationship between turbulence kinetic energy, and, aerosol and cloud droplet number concentration: Two-dimensional binning of N_d as a function of TKE and N_a for aerosol sizes greater than 0.1 µm.

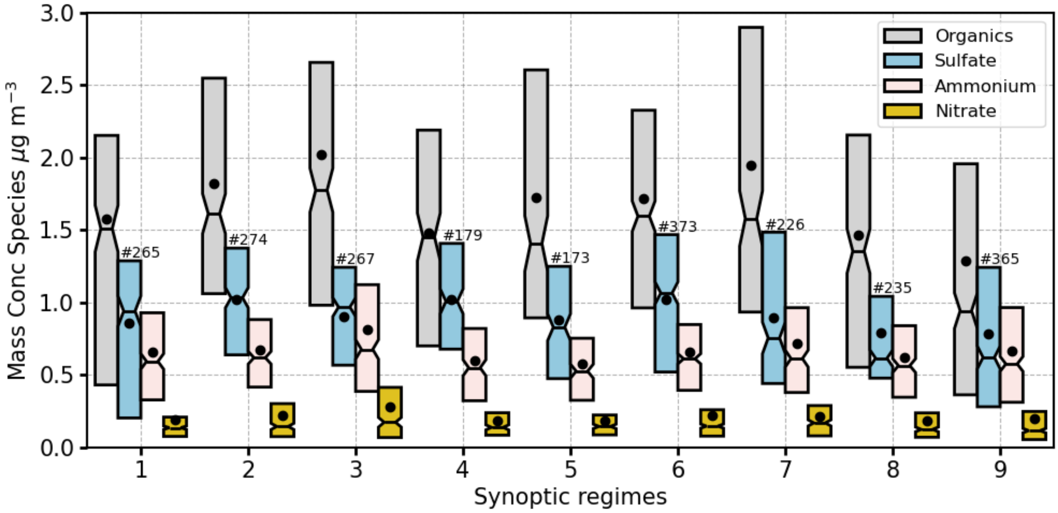

Figure 13: Mass concentration of aerosol composition at Scripps Pier for April to October 2023 for Organics (gray), sulfate (blue), ammonium (pink), and Nitrate (gold). *Notches (sometimes negligible) represent the 95% confidence interval of the median. The number of samples for each regime is shown on the figure.*

4. Summary and discussions

We classified the atmospheric circulation over the northeast Pacific coastal region using Self-Organizing Maps, with the goal of understanding how synoptic variability modulates changes in aerosol and cloud characteristics. Detailed MBL and local cloud and aerosol observations were provided by the ARM for the ground-based site at Scripps Pier in Southern California and GOES-18 satellite cloud products from SatCORPS during the ARM DOE Eastern Pacific Cloud Aerosol Precipitation Experiment (EPCAPE) campaign. We identify nine synoptic regimes, representing dominant meteorological patterns influencing coastal Southern California. The regimes can be interpreted in terms of the anticyclone evolution as follows: regime 4 features a relatively well-developed anticyclone at the center of the domain, with a cyclonic development at the northwestern edge of the NEP. The cyclone migrates southward, confining the anticyclone south of 35°N in regimes 1 and 2. This cyclone reaches its maximum southward extent for regime 3, featuring upward motions that are typical of midlatitude storms, conditions often associated with heavy precipitation episodes (Neiburger et al., 1961; Gershunov et al., 2019). As the low pressure moves eastward over land in regime 6, a new migrating anticyclone moves to the northwest, with strengthening and eastward displacement in regimes 9 and 8. Lastly, regime 7 captures the broadest spatial development of the high pressure, with ubiquitous subsidence.

For the coastal EPCAPE Scripps Pier site during April to October, 2023, MBL structure exhibits pronounced regime-dependent variability, reflecting contrasts in stability, humidity, and circulation. Regimes 8 and 9, with a well-developed anticyclone and its core north of Scripps Pier, feature the deepest boundary layer, the weakest MBL static stability, with regime 9 possessing the highest mean TKE and RH. In contrast, regime 7, with an anticyclone closer to Scripps Pier, is characterized by the shallowest boundary layer, the weakest turbulence, and a coupled MBL. While zonal winds remain modest (<5 m s^{-1}), stronger westerlies dominate in regimes 8–9, whereas meridional winds are predominantly northerlies in all regimes (1 to 8) but shifts to southerlies in regime 9, favoring advection of moist air from the ocean and resulting in increased clouds. Generally speaking, stable boundary layers are associated with the presence of shallow boundary layer, while the reduced stability in regimes 8–9 supports deeper, more turbulent layers, which are conditions typically associated with transition toward shallow cumulus convection (Teixeira et al., 2011; Zhou et al., 2015; Bretherton and Blossey, 2017).

The regional analysis of SatCORPS GOES-18 regime composites of LCF, N_d, LWP, and CTH reveal the influence of synoptic-scale meteorology on low-level clouds along the Southern California coast. Synoptic regimes with an anticyclone centered near 30–35°N and closer to coastal southern California (regimes 4 and 7) exhibit slightly reduced low-cloud amount (LCF <50%) and negative anomalies (–5 to –15%) along the coast, reflecting weak onshore flow and a configuration similar to that identified for Santa Ana offshore winds (Norris and Iacobellis, 2005). This decrease in cloud fraction for regimes 4 and 7 is associated with shallower clouds (CTH < 0.8 km) and reduction in LWP (LWP <50 g m^{-2}). Midlatitude cyclone influence (regimes 1–3) also suppresses low-cloud detection from passive satellite sensors due to overlying mid/high clouds, particularly during storm events (e.g., regime 3). Conversely, a northwest displacement of the anticyclone and a weak low-pressure pattern inland (regimes 6, 8, 9) appear to support extensive stratocumulus (LCF >75%) and positive LCF anomalies (~20%) under weaker subsidence along the coast and moist boundary layers. Regimes 6, 8, and 9 also feature a boundary layer deepening (CTH > 1 km) and a consistent increase in LWP. Regime 5 near climatological pattern shows intermediate cloud fraction (~50%) with minor negative anomalies.

https://doi.org/10.5194/egusphere-2026-933
Preprint. Discussion started: 6 March 2026

N_d exhibits strong coastal gradients for all regimes, exceeding 200 cm^{-3} nearshore and decreasing offshore, consistent with continental aerosol outflow and more active precipitation scavenging farther offshore (e.g. Wood et al., 2012). Regimes 3 and 6 show wider area of greater N_d and positive N_d anomalies (>20 cm^{-3}), however, sampling biases in regime 3 are possible due to the reduced satellite detection of MBL clouds, associated in part to the obscuration by middle and high level clouds (Fig. S2). On the other hand, wind strengthening and a flow that runs parallel to the coastline for regimes 7 – 9 appears to confine aerosol advection to a narrow coastal band, resulting in a drastic decrease in N_d of 100 cm^{-3} just 5˚ degrees west from Baja California (30˚N, 115˚W).

Comparisons between SatCORPS satellite derived and EPCAPE ground-based radar observations at Scripps Pier show that the satellite CTH agrees within about 100 m of radar measurements. The radar can detect small shallow clouds typically well below the inversion, which are too small to be resolved at the satellite pixel resolution, which causes satellites to report slightly higher cloud tops. Satellite and the ground-based microwave LWP agrees within 5–15 g m^{-2}. N_d derived from ground-based cloud-mode sun photometer derived cloud optical depth and microwave radiometer derived LWP, and satellite retrievals show similar range and pattern in variation for the synoptic regimes, though the satellite mean and medians are systematically higher. This N_d comparison also highlights the challenges of indirectly deriving N_d with remote sensing observations (e.g. Grosvenor et al., 2018). While N_d estimated from GOES-18 has the advantage of being derived with retrievals from a radiometrically consistent algorithm, the coarse pixel resolution (2 km) prevents the detection of small clouds. While ground-based retrievals are in principle more accurate, the need of combining data from 2 different instruments (microwave and visible radiometers) could result in significant noise in the estimated N_d, especially when biases in LWP or cloud optical depth are not properly characterized. Even though retrievals of cloud droplet effective radius are available from the sun-photometer and the multifilter rotating shadowband radiometer (MFRSR), the derivation of r_e from ground-based passive radiometers is more prone to uncertainties than cloud optical depth (e.g. Chiu et al, 2012). Given how critical N_d is for understanding aerosol effects on clouds, future field deployments would benefit from dedicated efforts of intercomparing and evaluating N_d products, especially when in-situ cloud microphysical observations are available.

Analysis of particle number concentrations at Scripps Pier reveals that the regime classification does not result in evident aerosol changes, possibly because the site is near multiple

https://doi.org/10.5194/egusphere-2026-933
Preprint. Discussion started: 6 March 2026

local pollution sources, while winds modestly change at the site during the period of study. Indeed, backtrajectories reveal predominantly coastal-parallel flow, with regime 7 featuring land influence, but minimal trajectory variability, suggesting that local sources and mesoscale processes are important for understanding aerosol variability (e.g., land–sea breeze). It is, however, noteworthy that the smallest statistically significant median $N_{a<0.1}$ and the smallest $N_{a<0.1}$ to $N_{a>0.1}$ ratio (~ 1) were observed for regime 6. This regime features the sharpest inversion jump ($\Delta\theta > 8$ K) and a relatively shallow boundary layer. This inversion strengthening is expected to be directly connected to a weakening of entrainment of free tropospheric air, and thus, hampering free tropospheric aerosol from being incorporated into the boundary layer, especially when fine (Aitken) mode aerosols dominates in the free troposphere (e.g. Covert et al., 1996).

CCN concentration at 0.2% supersaturation mirrors the changes in larger particle concentration, whereas CCN at 0.1% more closely matches the N_d values. These findings underscore the low values of supersaturation over the coastal region, and how this environmental constraint prevents more aerosols from being activated into droplets despite high aerosol concentrations. For instance, the lowest N_d in regime 2 appears to be partially explained by the low turbulence, as TKE reaches a minimum for that regime. Conversely, the highest TKE value for regime 9 are concomitant with high mean N_d and the N_d highest upper quartile. In a more general sense, the N_d drivers can be more explicitly observed in Figure 12, where the highest N_d occurs for both high aerosol concentration and high TKE. The analysis also suggests that due to weak values of supersaturations, a relatively small fraction of large mode aerosols (accumulation mode) is activated for concentrations smaller than 600 cm^{-3}, especially when the turbulence is modest. It follows that detailed information of updraft velocity and supersaturations are essential for understanding observational regressions between N_a–N_d, metric commonly referred to as the aerosol-cloud interactions (ACI) metric (Bellouin et al., 2019). Because specific meteorological regimes feature unique characteristics in terms of inversion strength, boundary layer deepening, and turbulence, the classification proposed here offers an alternative approach to the problem of disentangling the meteorological control over N_d variability, which is critical for understanding how aerosols impact clouds in the context of the aerosol indirect effect.

Code/Data availability

The Python implementation for generating Self-Organizing Maps was obtained from the MiniSom library, available at https://github.com/JustGlowing/minisom. The ARM EPCAPE measurements are available through https://adc.arm.gov/discovery/results/site_code::epc/start_date::2023-02-15/end_date::2024-02-14.

Acknowledgements

ARM EPCAPE measurements were obtained from the Atmospheric Radiation Measurement (ARM) Program sponsored by the U.S. Department of Energy, Office of Science, Office of Biological and Environmental Research, Climate and Environmental Sciences Division. This research was supported by ARM/ASR DOE funding DE-FOA-0002850.

Author Contributions

SC and DP designed the study. SC performed the analysis and drafted the manuscript with contributions from all the co-authors. CP and LR provided the ground-based aerosol and corrected CCN measurements. All co-authors participated in discussions and manuscript review.

Competing interests

Atleast one of the authors is member of the editorial board of ACP.

ARM EPCAPE data access:

Atmospheric Radiation Measurement (ARM) user facility. 2023. Active Remote Sensing of CLouds (ARSCL) product using Ka-band ARM Zenith Radars (ARSCLKAZRBND1KOLLIAS), 2023-02-15 to 2024-02-14, ARM Mobile Facility (EPC) La Jolla, CA; AMF1 (main site for EPCAPE on Scripps Pier) (M1). Compiled by K. Johnson, S. Giangrande and T. Toto. ARM Data Center. Data set accessed on 2025-05-18.

Atmospheric Radiation Measurement (ARM) user facility. 2023. Cloud optical depth retrieved from multi-channel sunphotometer (SPHOTCOD2CHIU), 2023-02-15 to 2024-02-13, ARM Mobile Facility (EPC) La Jolla, CA; AMF1 (main site for EPCAPE on Scripps Pier)

https://doi.org/10.5194/egusphere-2026-933
Preprint. Discussion started: 6 March 2026

(M1). Compiled by T. Fairless, S. Giangrande, C. and L. Ma. ARM Data Center. Data set accessed 2025-05-09.

Atmospheric Radiation Measurement (ARM) user facility. 2023. Balloon-Borne Sounding System (SONDEWNPN), 2023-02-15 to 2024-02-14, ARM Mobile Facility (EPC) La Jolla, CA; AMF1 (main site for EPCAPE on Scripps Pier) (M1). Compiled by E. Keeler, K. Burk and J. Kyrouac. ARM Data Center. Data set accessed 2025-04-01.

Atmospheric Radiation Measurement (ARM) user facility. 2023. MWR Retrievals with MWRRET Version 2 (MWRRET2TURN), 2023-02-15 to 2024-02-14, ARM Mobile Facility (EPC) La Jolla, CA; AMF1 (main site for EPCAPE on Scripps Pier) (M1). Compiled by K. Gaustad and D. Zhang. ARM Data Center. Data set accessed 2025-07-01.

Atmospheric Radiation Measurement (ARM) user facility. 2023. Airmass trajectories to support studies using ARM data (ARMTRAJPBL). 2023-03-01 to 2024-02-13, ARM Mobile Facility (EPC) La Jolla, CA; AMF1 (main site for EPCAPE on Scripps Pier) (M1). ARM Data Center. Data set accessed 2024-08-08.

Atmospheric Radiation Measurement (ARM) user facility. 2023. Ceilometer (CEIL10M), 2023-02-15 to 2024-02-14, ARM Mobile Facility (EPC) La Jolla, CA; Supplemental Facility 2 (Mt Soledad lab) (S2). Compiled by D. Zhang, V. Morris and B. Ermold. ARM Data Center. Data set accessed 2025-02-04.

References

Abel, M. R. and Hall, A.: Local and synoptic mechanisms causing Southern California's Santa Ana winds, *Clim. Dyn.*, 34, 847–857, https://doi.org/10.1007/s00382-009-0650-4, 2010.

Beddows, D. C. S., Dall'osto, M., and Harrison, R. M.: An enhanced procedure for the merging of atmospheric particle size distribution data measured using electrical mobility and time-of-flight analysers, *Aerosol Sci. Technol.*, 44, 11, https://doi.org/10.1080/02786826.2010.502159, 2010.

Bellouin, N., Quaas, J., Gryspeerdt, E., Kinne, S., Stier, P., Watson-Parris, D., et al.: Bounding global aerosol radiative forcing of climate change, *Rev. Geophys.*, 58, https://doi.org/10.1029/2019RG000660, 2020.

Berta, V. Z., Han, S., Atsushi, O., Dedrick, J. L., Maneenoi, N., and Russell, L. M.: Aerosol quantification products at Mt. Soledad and Scripps Pier during EPCAPE 2023–24, in: *Aerosol Microphysics and Chemical Measurements at Mt. Soledad and Scripps Pier during the Eastern Pacific Cloud Aerosol Precipitation Experiment (EPCAPE) from February 2023 to February 2024*, UC San Diego Library Digital Collections, https://doi.org/10.6075/J0WM1DSC, 2025.

Bishop, C. M.: Neural Networks for Pattern Recognition, Oxford University Press, New York, 1995.

Bretherton, C. S. and Blossey, P. N.: Understanding mesoscale aggregation of shallow cumulus convection using large-eddy simulation, *J. Adv. Model. Earth Syst.*, 9, 2798–2821, 2017.

https://doi.org/10.5194/egusphere-2026-933
Preprint. Discussion started: 6 March 2026

Bretherton, C. S., Wood, R., George, R. C., Leon, D., Allen, G., and Zheng, X.: Southeast Pacific stratocumulus clouds, precipitation and boundary layer structure sampled along 20°S during VOCALS-Rex, *Atmos. Chem. Phys.*, 10, 10639–10654, https://doi.org/10.5194/acp-10-10639-2010, 2010.

Chen, Y. C., Christensen, M., Stephens, G., et al.: Satellite-based estimate of global aerosol–cloud radiative forcing by marine warm clouds, *Nat. Geosci.*, 7, 643–646, https://doi.org/10.1038/ngeo2214, 2014.

Chiu, J. C., Marshak, A., Huang, C.-H., Várnai, T., Hogan, R., Giles, D. M., Holben, B. N., O'Connor, E., Knyazikhin, Y., and Wiscombe, W. J.: Cloud droplet size and liquid water path retrievals from zenith radiance measurements: examples from the Atmospheric Radiation Measurement Program and the Aerosol Robotic Network, *Atmos. Chem. Phys.*, 12, 10313–10329, https://doi.org/10.5194/acp-12-10313-2012, 2012.

Chiu, J. C., Huang, C., Marshak, A., Slutsker, I., Giles, D. M., Holben, B. N., Knyazikhin, Y., and Wiscombe, W. J.: Cloud optical depth retrievals from the Aerosol Robotic Network (AERONET) cloud mode observations, *J. Geophys. Res.*, 115, D14202, https://doi.org/10.1029/2009JD013121, 2010.

Christensen, M. W., Jones, W. K., and Stier, P.: Aerosols enhance cloud lifetime and brightness along the stratus-to-cumulus transition, *Proc. Natl. Acad. Sci. U.S.A.*, 117, 17591–17598, https://doi.org/10.1073/pnas.1921231117, 2020.

Clement, A. C., Burgman, R., and Norris, J. R.: Observational and model evidence for positive low-level cloud feedback, *Science*, 325, 460–464, https://doi.org/10.1126/science.1171255, 2009.

Clemesha, R. E. S., Gershunov, A., Iacobellis, S. F., and Cayan, D. R.: Daily variability of California coastal low cloudiness: A balancing act between stability and subsidence, *Geophys. Res. Lett.*, 44, 3330–3338, https://doi.org/10.1002/2017GL073075, 2017.

Cook, D. R. and Sullivan, R. C.: Eddy Correlation Flux Measurement System (ECOR) Instrument Handbook, U.S. Department of Energy, Atmospheric Radiation Measurement user facility, Richland, Washington, DOE/SC ARM-TR-052, 2025.

Covert, D. S., Kapustin, V. N., Bates, T. S., and Quinn, P. K.: Physical properties of marine boundary layer aerosol particles of the mid-Pacific in relation to sources and meteorological transport, *J. Geophys. Res.*, 101, D3, 6919–6930, https://doi.org/10.1029/95JD03068, 1996.

Dedrick, J. L., Osawa, A., Russell, L. M., Miller, M., Robinson, L., Chang, R., Williams, A. S., Berta, V. Z., Elavarasi, R., Petters, M. D., Wheeler, M., Han, S., Pelayo, C., Maneenoi, N., Lubin, D., Uin, J., Enekwizu, O., Zawadowicz, M., and Mayol-Bracero, O.:Quantitative estimates of cloud supersaturation and particle scavenging by urban coastal stratocumulus during EPCAPE, submitted to *J. Atmos. Sci.*, 2026.

Feng, Y., Lindenmaier, I., Theisen, A., Wang, D., Collis, S., Tian, J., Silber, I., Gupta, S., Zhang, D., Mather, J., Comstock, J., Jackson, R., O'Brien, J., and Raut, B.: ARM FY2025 Radar Plan, ed. by Robert Stafford, ARM user facility, DOE/SC-ARM-TR-308, https://doi.org/10.2172/2482518, 2024.

Gaustad, K. L. and Turner, D. D.: MWRRET Value-Added Product: The Retrieval of Liquid Water Path and Precipitable Water Vapor from Microwave Radiometer (MWR) Data Sets, ARM-TR-081.1, U.S. Department of Energy, 2009.

Gershunov, A., Shulgina, T., Clemesha, R. E., Guirguis, K., Pierce, D. W., Dettinger, M. D., and Cayan, D. R.: Precipitation regime change in Western North America: The role of atmospheric rivers, *Sci. Rep.*, 9, 9944, https://doi.org/10.1038/s41598-019-46169-w, 2019.

Grosvenor, D. P., Sourdeval, O., Zuidema, P., Ackerman, A., Alexandrov, M. D., Bennartz, R., et al.: Remote sensing of droplet number concentration in warm clouds: A review of the current state of knowledge and perspectives, *Rev. Geophys.*, 56, 409–453, https://doi.org/10.1029/2017RG000593, 2018.

Gryspeerdt, E., Quaas, J., and Bellouin, N.: Constraining the aerosol influence on cloud fraction, *J. Geophys. Res. Atmos.*, 121, 3566–3583, https://doi.org/10.1002/2015JD023744, 2016.

Han, S., Williams, A. S., Russell, L. M., Berta, V. Z., Dedrick, J. L., Pelayo, C., Maneenoi, N., Osawa, A., Silber, I., Zhang, D., Zawadowicz, M. A., and Sedlacek III, A. J.: Nearby Sites Show Similar Upwind Sources and Differing Semivolatile Concentrations in Coastal Aerosol Particles, *ACS ES&T Air*, 2, 2824–2837, https://doi.org/10.1021/acsestair.5c00191, 2025.

Hartmann, D., Ockert-Bell, M. E., and Michelsen, M. L.: The effect of cloud type on Earth's energy balance: Global analysis, *J. Climate*, 5, 1281–1304, https://doi.org/10.1175/1520-0442(1992)005<1281:TEOCTO>2.0.CO;2, 1992.

Haykin, S.: Neural Networks and Learning Machines, 3rd Edn., Pearson Education, Inc., McMaster University, Hamilton, available at: http://dai.fmph.uniba.sk/courses/NN/haykin.neural-networks.3ed.2009.pdf, 2009.

Haykin, S.: Neural Networks: A Comprehensive Foundation, 2nd Edn., Prentice Hall, 1999.
Hersbach, H., Bell, B., Berrisford, P., Hirahara, S., Horányi, A., Muñoz-Sabater, J., et al.: The ERA5 global reanalysis, *Q. J. R. Meteorol. Soc.*, 146, 1999–2049, https://doi.org/10.1002/qj.3803, 2020.

Hewitson, B. and Crane, R.: Self-organizing maps: applications to synoptic climatology, *Clim. Res.*, 22, 13–26, https://doi.org/10.3354/cr022013, 2002.

Husar, R. B. and Patterson, D. E.: Regional scale air pollution: Sources and effects, *Ann. N. Y. Acad. Sci.*, 338, 399–417, https://doi.org/10.1111/j.1749-6632.1980.tb17136.x, 1980.

Husar, R., Patterson, D., Blumenthal, D., White, W., and Smith, T.: Three-dimensional distribution of air pollutants in the Los Angeles Basin, *J. Appl. Meteorol. Climatol.*, 16, 1089–1096, https://doi.org/10.1175/1520-0450-16.10.1089, 1977.

Iacobellis, S. F. and Cayan, D. R.: The variability of California summertime marine stratus: Impacts on surface air temperatures, *J. Geophys. Res. Atmos.*, 118, 9105–9122, https://doi.org/10.1002/jgrd.50652, 2013.

Jiang, N., Kim, N., Dirks, K., and Luo, K.: Classification of synoptic weather types using the self-organising map and its application to climate and air quality data visualisation, *Weather and Climate*, 33, 52–75, 2013.

Jones, C. R., Bretherton, C. S., and Leon, D.: Coupled vs. decoupled boundary layers in VOCALS-REx, *Atmos. Chem. Phys.*, 11, 7143–7153, https://doi.org/10.5194/acp-11-7143-2011, 2011.

Juliano, T. W. and Lebo, Z. J.: Linking large-scale circulation patterns to low-cloud properties, *Atmos. Chem. Phys.*, 20, 7125–7138, https://doi.org/10.5194/acp-20-7125-2020, 2020.

Keeler, E.: Balloon-Borne Sounding System (SONDE) Instrument Handbook, ed. by Robert Stafford, U.S. Department of Energy, DOE/SC-ARM/TR-029, https://doi.org/10.2172/1020712, 2025.

Klein, S. A. and Hartmann, D. L.: The seasonal cycle of low stratiform clouds, *J. Climate*, 6, 1587–1606, 1993.

Klein, S. A., Hartmann, D. L., and Norris, J. R.: On the relationships among low-cloud structure, sea surface temperature, and atmospheric circulation in the summertime northeast Pacific, *J. Climate*, 10, 2550–2563, 1997.

Kohonen, T.: The self-organizing map, *Proc. IEEE*, 78, 1464–1480, 1990.

Kohonen, T.: Self-Organizing Maps, 3rd Edn., Springer-Verlag, Berlin, Heidelberg, New York, 501 pp., https://doi.org/10.1007/978-3-642-56927-2, 2001.

Kohonen, T.: Self-organized formation of topologically correct feature maps, *Biol. Cybern.*, 43, 59–69, https://doi.org/10.1007/BF00337288, 1982.

Krzywinski, M. and Altman, N.: Points of significance: Comparing samples – part I, *Nat. Methods*, 11, 215–216, https://doi.org/10.1038/nmeth.2858, 2014.

Lebassi-Habtezion, B., González, J., and Bornstein, R.: Modeled large-scale warming impacts on summer California coastal-cooling trends, *J. Geophys. Res.*, 116, D20114, https://doi.org/10.1029/2011JD015759, 2011.

Lewis, E. R.: Marine ARM GPCI Investigation of Clouds (MAGIC) Field Campaign Report, U.S. Department of Energy, https://doi.org/10.2172/1343577, 2016.

Lu, R. and Turco, R. P.: Air pollutant transport in a coastal environment – II. Three-dimensional simulations over Los Angeles basin, *Atmos. Environ.*, 29, 1499–1518, https://doi.org/10.1016/1352-2310(95)00015-Q, 1995.

Lu, R. and Turco, R. P.: Air pollutant transport in a coastal environment. Part I: Two-dimensional simulations of sea-breeze and mountain effects, *J. Atmos. Sci.*, 51, 2285–2308, https://doi.org/10.1175/1520-0469(1994)051<2285:APTIAC>2.0.CO;2, 1994.

Maneenoi, N., Russell, L., Han, S., Dedrick, J. L., Williams, A., Berta, V. Z., Pelayo, C., et al.: Photochemical and cloud and aerosol aqueous contributions to regionally-emitted shipping and biogenic non-sea-salt sulfate aerosol in coastal California, *ACS ES&T Air*, 2, 648–664, https://doi.org/10.1021/acsestair.4c00352, 2025.

Minnis, P., Sun-Mack, S., Chen, Y., Chang, F.-L., Yost, C. R., Smith, W. L. Jr., Heck, P. W., Arduini, R. F., Bedka, S. T., Yi, Y., Hong, G., Jin, Z., Painemal, D., Palikonda, R., Scarino, B., Spangenberg, D. A., Smith, R. A., Trepte, Q. Z., Yang, P., and Xie, Y.:CERES MODIS cloud product retrievals for Edition 4, Part I: Algorithm changes, *IEEE Trans. Geosci. Remote Sens.*, 51, 2744–2780, https://doi.org/10.1109/TGRS.2020.3008866, 2021.

Minnis, P., Trepte, Q. Z., Sun-Mack, S., Chen, Y., Doelling, D. R., Young, D. F., Spangenberg, D. A., Miller, W. F., Wielicki, B. A., Brown, R. R., and Gibson, S. C.: Cloud detection in nonpolar regions for CERES using TRMM VIRS and Terra and Aqua MODIS data, *IEEE Trans. Geosci. Remote Sens.*, 46, 3857–3884, 2008.

Minnis, P., Sun-Mack, S., Young, D. F., Heck, P. W., Garber, D. P., Chen, Y., Spangenberg, D. A., Arduini, R. F., Trepte, Q. Z., Smith, W. L., and Ayers, J. K.: CERES edition-2 cloud property retrievals using TRMM VIRS and Terra and Aqua MODIS data – Part I: Algorithms, *IEEE Trans. Geosci. Remote Sens.*, 49, 4374–4400, 2011.

Minnis, P., Sun-Mack, S., Smith, W. L. Jr., Trepte, Q. Z., Hong, G., Chen, Y., Yost, C. R., Chang, F.-L., Smith, R. A., Heck, P. W., and Yang, P.: VIIRS Edition 1 Cloud Properties for CERES, Part 1: Algorithm Adjustments and Results, *Remote Sens.*, 15, 578, https://doi.org/10.3390/rs15030578, 2023.

Morris, V. R.: Ceilometer Instrument Handbook, DOE/SC-ARM-TR-020, U.S. Department of Energy, https://doi.org/10.2172/1036530, April 2016.

Myers, T. A. and Norris, J. R.: Observational evidence that enhanced subsidence reduces subtropical marine boundary layer cloudiness, *J. Climate*, 26, 7507–7524, https://doi.org/10.1175/JCLI-D-12-00736.1, 2013.

Neiburger, M., Johnson, D. S., and Chien, C.-W.: Studies of the Structure of the Atmosphere over the Eastern Pacific Ocean in the Summer, University of California Press, 94 pp., 1961.

Newsom, R. K., Sivaraman, C., Shippert, T. R., and Riihimaki, L. D.: Doppler Lidar Vertical Velocity Statistics Value-Added Product, DOE/SC-ARM-TR-149, U.S. Department of Energy, Atmospheric Radiation Measurement user facility, Richland, Washington, 2025.

Norris, J. R. and Iacobellis, S. F.: North Pacific cloud feedbacks inferred from synoptic-scale dynamic and thermodynamic relationships, *J. Climate*, 18, 4862–4878, https://doi.org/10.1175/JCLI3558.1, 2005.

Painemal, D.: Global estimates of changes in shortwave low-cloud albedo and fluxes due to variations in cloud droplet number concentration derived from CERES-MODIS satellite sensors, *Geophys. Res. Lett.*, 45, 9288–9296, https://doi.org/10.1029/2018GL078880, 2018.

Painemal, D., Chiu, J.-Y. C., Minnis, P., Yost, C., Zhou, X., Cadeddu, M., Eloranta, E., Lewis, E. R., Ferrare, R., and Kollias, P.: Aerosol and cloud microphysics covariability in the northeast Pacific boundary layer estimated with ship-based and satellite remote sensing observations, *J. Geophys. Res. Atmos.*, 122, 2403–2418, https://doi.org/10.1002/2016JD025771, 2017.

Painemal, D., Minnis, P., and Nordeen, M.: Aerosol variability, synoptic-scale processes, and their link to the cloud microphysics over the northeast Pacific during MAGIC, *J. Geophys. Res. Atmos.*, 120, 5122–5139, https://doi.org/10.1002/2015JD023175, 2015.

Painemal, D., Smith, W. L. Jr., Gupta, S., Moore, R., Cairns, B., McFarquhar, G. M., and O'Brien, J.: Can we rely on satellite visible/infrared microphysical retrievals of boundary layer clouds in partially cloudy scenes? Implications for climate research, *Geophys. Res. Lett.*, 52, e2024GL113825, https://doi.org/10.1029/2024GL113825, 2025.

Painemal, D. and Zuidema, P.: Assessment of MODIS cloud effective radius and optical thickness retrievals over the Southeast Pacific with VOCALS-REx in situ measurements, *J. Geophys. Res.*, 116, D24206, https://doi.org/10.1029/2011JD016155, 2011.

Painemal, D. and Zuidema, P.: The first aerosol indirect effect quantified through airborne remote sensing during VOCALS-REx, *Atmos. Chem. Phys.*, 13, 917–931, https://doi.org/10.5194/acp-13-917-2013, 2013a.

Painemal, D., Minnis, P., Sun-Mack, S., and Wood, R.: The impact of horizontal heterogeneities, cloud fraction, and liquid water path retrievals on MODIS droplet effective radius retrievals, *J. Geophys. Res. Atmos.*, 118, 6564–6575, https://doi.org/10.1002/jgrd.50374, 2013b.

Painemal, D., Chellappan, S., Smith, W. L. Jr., Spangenberg, D., Park, J. M., Ackerman, A., Chen, J., Crosbie, E., Ferrare, R., Hair, J., Kirschler, S., Li, X.-Y., McComiskey, A., Moore, R. H., Sanchez, K., Sorooshian, A., Tornow, F., Voigt, C., Wang, H., Winstead, E., Zeng, X., Ziemba, L., and Zuidema, P.: Wintertime synoptic patterns of midlatitude boundary layer clouds over the western North Atlantic: Climatology and insights from in-situ ACTIVATE observations, *J. Geophys. Res. Atmos.*, 128, e2022JD037725, https://doi.org/10.1029/2022JD037725, 2023.

Parish, T. R.: Forcing of the summertime low-level jet along the California coast, *J. Appl. Meteorol. Climatol.*, 39, 2421–2433, 2000.

Pearce, J. L., Waller, L. A., Chang, H. H., et al.: Using self-organizing maps to develop ambient air quality classifications: a time series example, *Environ. Health*, 13, 56, https://doi.org/10.1186/1476-069X-13-56, 2014.

Raphael, M. N.: The Santa Ana winds of California, *Earth Interact.*, 7, 1–13, https://doi.org/10.1175/1087-3562(2003)007<0001:TSAWOC>2.0.CO;2, 2003.

Russell, L. M., Miller, M., Lubin, D., Ackerman, A., Silber, I., Fridlind, A., Eloranta, E., Witte, M., Muelmenstaedt, J., Lebsock, M., Burrows, S., Painemal, D., Aiken, A., Chang, R., Wang, D., Liggio, J., Petters, M., Wheeler, M., et al.: EPCAPE Field Campaign, Final Campaign Report, DOE/SC-ARM-25-010, U.S. Department of Energy, April 2025.

Sheridan, S. C. and Lee, C. C.: The self-organizing map in synoptic climatological research, *Prog. Phys. Geogr.*, 35, 109–119, 2011.

Shilling, J. and Levin, M.: ACSM, corrected for composition-dependent collection efficiency (ACSMCDCE), ARM Data Center, https://doi.org/10.5439/1641833, 2024.

https://doi.org/10.5194/egusphere-2026-933
Preprint. Discussion started: 6 March 2026

Shilling, J. E. and Levin, M. S.: Scanning Mobility Particle Sizer (SMPS)-Aerodynamic Particle Sizer (APS) Merged Size Distribution (mergedsmpsaps) Value-Added Product Report, DOE/SC-ARM-TR-294, U.S. Department of Energy, Atmospheric Radiation Measurement user facility, Richland, Washington, 2023.

Silber, I., Comstock, J. M., Kieburtz, M. R., and Russell, L. M.: ARMTRAJ: a set of multipurpose trajectory datasets augmenting the Atmospheric Radiation Measurement (ARM) user facility measurements, *Earth Syst. Sci. Data*, 17, 29–42, https://doi.org/10.5194/essd-17-29-2025, 2025.

Sorooshian, A., and Coauthors: Aerosol–Cloud–Meteorology Interaction Airborne Field Investigations: Using Lessons Learned from the U.S. West Coast in the Design of ACTIVATE off the U.S. East Coast, *Bull. Am. Meteorol. Soc.*, 100, 1511–1528, https://doi.org/10.1175/BAMS-D-18-0100.1, 2019.

Sullivan, R. C., Billesbach, D. P., Biraud, S., Chan, S., Hart, R., Keeler, E., Kyrouac, J., Pal, S., Pekour, M., Sullivan, S. L., Theisen, A., Tuftedal, M., and Cook, D. R.: Over three decades, and counting, of near-surface turbulent flux measurements from the Atmospheric Radiation Measurement (ARM) user facility, *Earth Syst. Sci. Data*, 17, 5007–5038, https://doi.org/10.5194/essd-17-5007-2025, 2025.

Teixeira, J., et al.: Tropical and sub-tropical cloud transitions in weather and climate prediction models: The GCSS/WGNE Pacific Cross-section Intercomparison (GPCI), *J. Clim.*, 24, 5223–5256, https://doi.org/10.1175/2011JCLI3672.1, 2011.

Turner, D. D., Clough, S. A., Liljegren, J. C., Clothiaux, E. E., Cady-Pereira, K. E., and Gaustad, K. L.: Retrieving liquid water path and precipitable water vapor from the Atmospheric Radiation Measurement (ARM) microwave radiometers, *IEEE Trans. Geosci. Remote Sens.*, 45, 3680–3690, https://doi.org/10.1109/TGRS.2007.903703, 2007.

Vesanto, J. and Alhoniemi, E.: Clustering of the self-organizing map, *IEEE Trans. Neural Netw.*, 11, 586–600, https://doi.org/10.1109/72.846731, 2000.

Vettigli, G.: MiniSom: Minimalistic and Numpy-Based Implementation of the Self Organizing Map, available at: https://github.com/JustGlowing/minisom/, 2018.

Weaver, C. P. and Ramanathan, V.: Relationships between large-scale vertical velocity, static stability, and cloud radiative forcing over Northern Hemisphere extratropical oceans, *J. Climate*, 10, 2871–2887, https://doi.org/10.1175/1520-0442(1997)010<2871:RBLSVV>2.0.CO;2, 1997.

Widener, K., Bharadwaj, N., and Johnson, K.: Ka-Band ARM Zenith Radar Handbook, DOE/SC-ARM/TR-106, https://doi.org/10.2172/1035855, 2012.

Wood, R.: Stratocumulus clouds, *Mon. Weather Rev.*, 140, 2373–2423, https://doi.org/10.1175/mwr-d-11-00121.1, 2012.

Wood, R. and Bretherton, C. S.: Boundary layer depth, entrainment, and decoupling in the cloud-capped subtropical and tropical marine boundary layer, *J. Climate*, 17, 3576–3588, https://doi.org/10.1175/1520-0442(2004)017<3576:BLDEAD>2.0.CO;2, 2004.

Wood, R., Leon, D., Lebsock, M., Snider, J., and Clarke, A. D.: Precipitation driving of droplet concentration variability in marine low clouds, *J. Geophys. Res.*, 117, D19210, https://doi.org/10.1029/2012JD018305, 2012.

Zhang, J., Zhou, X., Goren, T., and Feingold, G.: Albedo susceptibility of northeastern Pacific stratocumulus: the role of covarying meteorological conditions, *Atmos. Chem. Phys.*, 22, 861–880, https://doi.org/10.5194/acp-22-861-2022, 2022.

Zheng, Y., Rosenfeld, D., and Li, Z.: Sub-cloud turbulence explains cloud-base updrafts for shallow cumulus ensembles: First observational evidence, *Geophys. Res. Lett.*, 48, e2020GL091881, https://doi.org/10.1029/2020GL091881, 2021.

Zhou, C., Zelinka, M. D., Dessler, A. E., and Klein, S. A.: The relationship between interannual and long-term cloud feedbacks, *Geophys. Res. Lett.*, 42, 10463–10469, https://doi.org/10.1002/2015GL066698, 2015.